



A 100 Mpc² Structure Traced by Hyperluminous Galaxies around a Massive $z = 2.85$ Protocluster

George C.P. Wang¹ , Scott C. Chapman^{1,2,3,4} , Nikolaus Sulzenauer⁵ , Frank Bertoldi⁶ , Christopher C. Hayward⁷ , Ryley Hill¹ , Satoshi Kikuta⁸ , Yuichi Matsuda^{8,9} , Douglas Rennehan⁷ , Douglas Scott¹ , Ian Smail¹⁰ , and Charles C. Steidel¹¹

¹ Department of Physics and Astronomy, University of British Columbia, 6225 Agricultural Road, Vancouver, V6T 1Z1, Canada; georgecpwang@phas.ubc.ca

² Department of Physics and Atmospheric Science, Dalhousie University, 6310 Coburg Road, B3H 4R2, Halifax, Canada

³ Eureka Scientific Inc, Oakland, CA 94602, USA

⁴ National Research Council, Herzberg Astronomy and Astrophysics, 5071 West Saanich Road, Victoria, V9E 2E7, Canada

⁵ Max-Planck-Institut für Radioastronomie, Auf dem Hügel 69, D-53121 Bonn, Germany

⁶ Argelander-Institut für Astronomie, Auf dem Hügel 71, D-53121 Bonn, Germany

⁷ Center for Computational Astrophysics, Flatiron Institute, 162 Fifth Avenue, New York, NY 10010, USA

⁸ National Astronomical Observatory of Japan, 2-21-1, Osawa, Mitaka, Tokyo 181-8588, Japan

⁹ Graduate University for Advanced Studies (SOKENDAI), 2-21-1 Osawa, Mitaka, Tokyo 181-8588, Japan

¹⁰ Centre for Extragalactic Astronomy, Department of Physics, Durham University, South Road, Durham DH1 3LE, UK

¹¹ Cahill Center for Astronomy and Astrophysics, California Institute of Technology, MC249-17, Pasadena, CA 91125, USA

Received 2024 June 24; revised 2025 February 7; accepted 2025 February 13; published 2025 April 7

Abstract

We present wide-field mapping at 850 μm and 450 μm of the $z = 2.85$ protocluster in the HS 1549+19 field using the Submillimetre Common-User Bolometer Array 2. Spectroscopic follow-up of 18 bright sources selected at 850 μm , using the Northern Extended Millimeter Array and Atacama Large Millimeter/submillimeter Array, confirms that the majority lie near $z \simeq 2.85$ and are likely members of the structure. Interpreting the spectroscopic redshifts as distance measurements, we find that the submillimeter galaxies (SMGs) span 123 pMpc² in the plane of the sky and demarcate a 3600 pMpc³ “pancake”-shaped structure in three dimensions. We find that the high star formation rates of these SMGs result in a total star formation rate of 20,000 $M_{\odot} \text{yr}^{-1}$ from just the brightest galaxies in the protocluster. These rapidly star-forming SMGs can be interpreted as massive galaxies growing rapidly at large clustercentric distances before collapsing into a virialized structure. We find that the SMGs trace the Ly α surface density profile. Comparison with simulations suggests that HS 1549+19 could be building a structure comparable to the most massive clusters in the present-day Universe.

Unified Astronomy Thesaurus concepts: [High-redshift galaxy clusters \(2007\)](#); [High-redshift galaxies \(734\)](#); [Cosmic web \(330\)](#)

1. Introduction

Massive galaxy clusters—collections of gravitationally bound galaxies—are now found as early as 3 billion years after the Big Bang and contain stars that formed at even earlier epochs (S. A. Stanford et al. 2012; T. Wang et al. 2016; A. B. Mantz et al. 2018). The high-redshift progenitors of these galaxy clusters, termed “protoclusters,” represent the highest dark matter overdensities at their epoch. While their observational signatures are less well-defined than the hot intracluster medium of virialized clusters, protoclusters contain extremely massive galaxies that can be observed as luminous starbursts (with star formation rates (SFRs) $> 100 M_{\odot} \text{yr}^{-1}$; C. M. Casey et al. 2015).

Galaxy evolution is known to be accelerated in regions with high overdensities—many studies have demonstrated enhanced star formation rates and a reversal of the star formation–density relation (star-forming galaxies prefer low-density environments) at $z > 1.5$ in galaxy clusters (D. Elbaz et al. 2007, 2011; K.-V. H. Tran et al. 2008; E. A. Cooke et al. 2019; I. Smail 2024). Exceptionally high levels of star formation have been found in the centers of clusters, reaching SFR surface densities

(SFRDs) of more than $2000 M_{\odot} \text{yr}^{-1} \text{Mpc}^{-2}$ at $z = 2\text{--}3$ (H. Umehata et al. 2015), and even higher at redshifts greater than 4 (T. B. Miller et al. 2018; I. Oteo et al. 2018). The reversal of the $z < 1.5$ trend in SFRD suggests that massive cluster galaxies may form the bulk of their stars in protoclusters around redshift 2, prior to their virialization (I. Smail 2024).

Performing surveys of the gas and dust in $z > 2$ protoclusters is of emerging importance (C. M. Casey 2016). Bright submillimeter galaxies (SMGs; typically $S_{850} > 5 \text{ mJy}$; S. C. Chapman et al. 2005) are believed to be galaxies seen at a moment when they are rapidly building up their stellar mass (e.g., I. Smail et al. 2004; U. Dudzevičiūtė et al. 2020).

In the HS 1549+19 field, a protocluster has been identified with significant galaxy overdensity traced by Ly α -emitting galaxies (LAEs) and UV continuum-selected galaxies, revealing a filamentary structure in the early Universe at a redshift of $z \approx 2.85$ when the Universe was 2.3 Gyr old (C. C. Steidel et al. 2011; S. Kikuta et al. 2019; K. M. Lacaille et al. 2019).

The HS 1549+19 (henceforth HS 1549) survey field at redshift 2.85 contains the strongest galaxy overdensity found in the Keck Baryonic Structure Survey (G. C. Rudie et al. 2012; R. E. Mostardi et al. 2013), even exceeding well-studied protoclusters such as SSA 22 at $z = 3.09$ (C. C. Steidel et al. 2000) or the Spiderweb protocluster at $z = 2.16$ (H. Dannerbauer et al. 2014). Using Ly α -emitting galaxies imaged with Subaru’s Hyper Suprime-Cam, the extended environment of this protocluster has been mapped

with unprecedented detail over a degree-diameter field, corresponding to projected distances of 30 pMpc^{12,13} (S. Kikuta et al. 2019). This map covers the full density distribution of all the subregions that are likely to collapse and become a Coma-type rich galaxy cluster ($>10^{15} M_{\odot}$) at redshift zero (Y.-K. Chiang et al. 2014).

In this paper, we report on 18 SMGs spectroscopically confirmed at $z \approx 2.85$ with Northern Extended Millimeter Array (NOEMA) band-1 and band-3 observations from initial Submillimetre Common User Bolometer Array 2 (SCUBA-2) 850 μm observations. In Section 2 we describe the photometry and spectroscopy that facilitated the detection of galaxies in the HS 1549 protocluster. In Section 3, we describe the fitting of spectral lines, the SMGs’ membership, and the properties derived from these lines. In Section 4 we present our findings on the distribution of the SMGs across the protocluster and the resulting structural shape. Section 5 discusses the star formation rates in comparison with the LAEs and to other protocluster–SMG surveys and how HS 1549 compares with dark matter simulations. We summarize and conclude the paper in Section 6.

The paper assumes a standard Λ CDM model with cosmological parameters taken from Planck Collaboration et al. (2020). In cases where we need to model the spectral energy distribution (SED), we apply a modified blackbody function with a dust temperature of 40 K and a median dust emissivity index of 2 (T. R. Greve et al. 2012; A. M. Swinbank et al. 2014; E. da Cunha et al. 2015).

2. Observations

2.1. JCMT/SCUBA-2 Observations

The James Clerk Maxwell Telescope’s (JCMT) SCUBA-2 (W. S. Holland et al. 2013) instrument was used to map the HS 1549 field, encompassing the structure around the bright central quasi-stellar object (QSO). The project aimed to cover all regions of the highest overdensity in LAEs (S. Kikuta et al. 2019). The map covers a total area of 0.24 deg² at 850 μm (Figure 1) and 0.18 deg² at 450 μm . SCUBA-2 previously observed the central core region (K. M. Lacaille et al. 2019), and these data were combined with our new map. There are a few outlying regions with comparable LAE overdensities that we have yet to map with SCUBA-2.

The SCUBA-2 observations were conducted in grade 2 weather conditions ($\tau_{225 \text{ GHz}} < 0.08$) over six nights between 2015 May 23 and October 15, totaling 15 hr of on-sky integration in individual scans of 30 minutes. Standard 3’ diameter “daisy” mapping patterns were used, which kept the pointing center on one of the four SCUBA-2 subarrays at all times during the exposure. The full map was constructed using a mosaic pattern of these daisy pointings.

Data reduction followed standard recipes (J. E. Geach et al. 2017), with individual scans of 30 minutes reduced using the dynamic iterative map-maker of the SMURF package (T. Jenness et al. 2009; E. L. Chapin et al. 2013), flat-fielding, and then solving for model components assumed to make up the bolometer signals (atmospheric, astronomical, and noise terms). The signal from each bolometer’s time stream was then regridded onto a

map, with the contribution to a given pixel weighted according to its time-domain variance. Since we are interested in extragalactic point sources, we applied a beam-matched filter to improve point-source detectability, resulting in a map that is convolved with an estimate of the 850 μm beam.

The 850 μm map has an average depth of $1.0^{+0.9}_{-0.2}$ mJy beam⁻¹ rms outside the deep core region (K. M. Lacaille et al. 2019) and the 450 μm map has a depth of $11.8^{+30.2}_{-6.1}$ mJy beam⁻¹ rms. The smaller coverage and over 10 times shallower 450 μm map make these data less useful for characterizing the SMGs, which leads us to search for submillimeter-bright sources at 850 μm with 450 μm flux densities reported only when available.

2.2. NOEMA Observations

From the SCUBA-2 map, we selected a flux-limited sample of 25 sources with brightnesses greater than 8 mJy at 850 μm for spectroscopic follow-up with the IRAM NOEMA interferometer to identify SMGs lying at $z \approx 2.85$ in the protocluster. The central core region was previously followed up with the Submillimetre Array at 850 μm and NOEMA at 3 mm (K. M. Lacaille et al. 2019). These studies resolved two $S_{850} > 8$ mJy sources from the central blended SCUBA-2 source and detected CO(3–2) lines with NOEMA, both lying at $z \approx 2.85$, along with two nearby $S_{850} \approx 5$ mJy sources. Our final NOEMA follow-up sample of $S_{850} > 8$ mJy sources in the wider field is thus reduced to 21.

Observations were obtained in two observing programs using NOEMA/PolyFix in 2020 and 2021, with Project IDs W20DD (for the 3 mm follow-up of CO(3–2)) and W21DH (for the 1.4 mm follow-up of CO(7–6)). 21 targets were observed at 3 mm, with spectral setups of two 8 GHz sidebands (26,000 km s⁻¹ per sideband) and an integration time of 1 hr per setup using the combined “CD” configuration, which is suitable for low-resolution detection experiments. The 1.4 mm program then targeted 14 sources with CO(3–2) line candidates found from the first program.

Reduction of the data was carried out using the standard Grenoble Image and Line Data Analysis Software (GILDAS).¹⁴ The raw data were calibrated using standard pipelines, with bad visibilities flagged and removed in the process, resulting in calibrated uv tables. The uv visibilities were then imaged using the GILDAS MAPPING pipeline. We used the Högbom algorithm (J. A. Högbom 1974) to clean the data products and deconvolve the telescope’s beam from the image. The results are data cubes in the image plane, with frequency bins of 20 MHz in width.

The 1.4 mm and 3.3 mm observations have an average depth of 1.20 mJy per channel and 0.69 mJy per channel, respectively. The average continuum sensitivity is 43 μJy at 1.4 mm and 25 μJy at 3.3 mm. At 3.3 mm the continuum emission falls to a level similar to that of our sensitivity (we quote the 3.3 mm continuum measurements in Table 1 for completeness). The $z \approx 2.85$ redshifted CO(3–2) and CO(7–6) spectral transitions are located in their receivers’ upper and lower sidebands, respectively.

2.3. ALMA Observations

The Atacama Large Millimeter/Submillimeter Array (ALMA) was used to map the HS 1549 core region in Band

¹² cMpc or Mpc are comoving megaparsecs, the distance between objects factoring out the expansion of the Universe.

¹³ pMpc are proper megaparsecs, the physical distance between objects, or cMpc/(1 + z).

¹⁴ <http://www.iram.fr/IRAMFR/GILDAS>

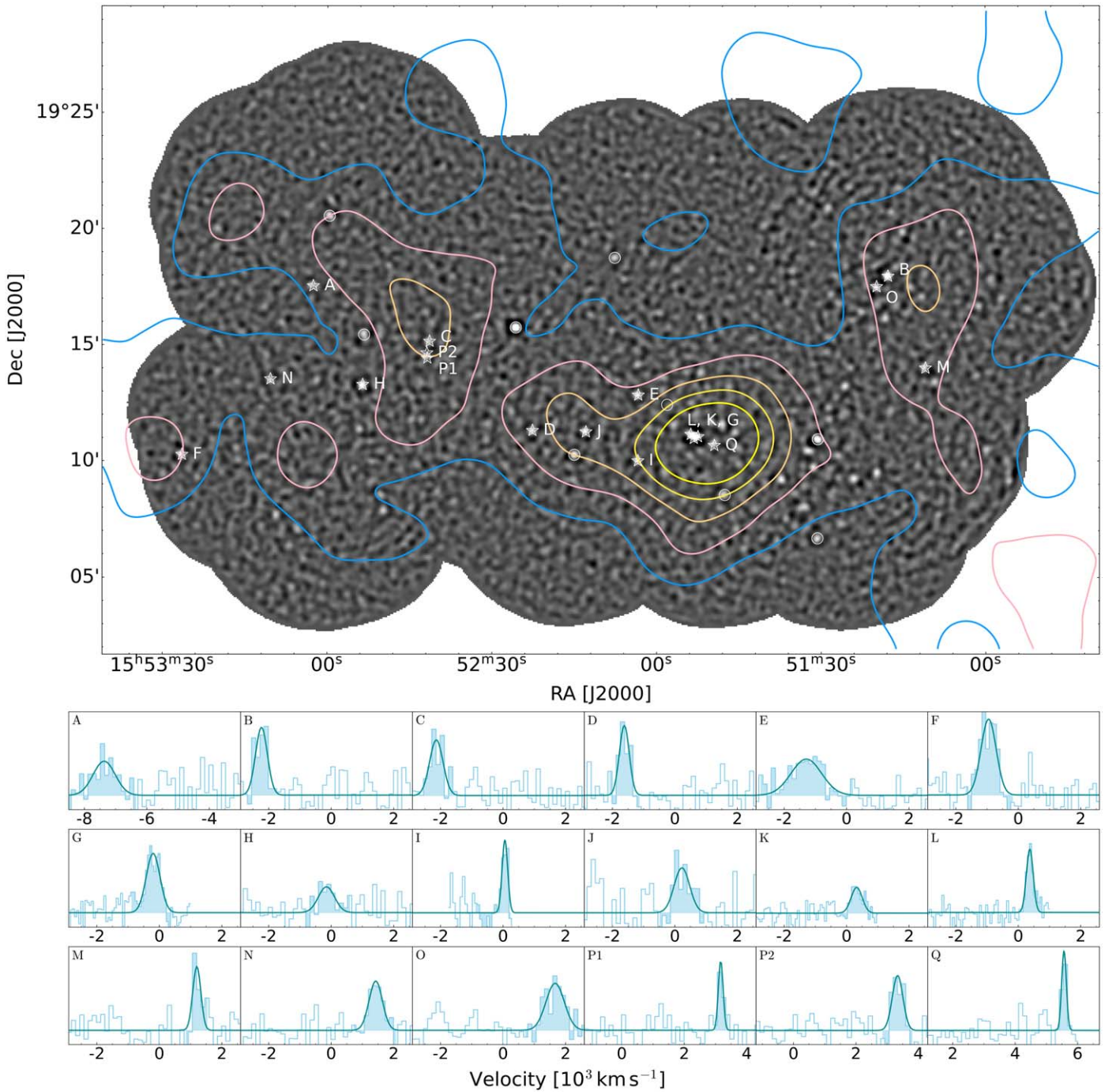


Figure 1. Overview of the protocluster HS 1549 and individual galaxy members. Top: the 850 μm SCUBA-2 map with LAE surface density contours (S. Kikuta et al. 2019) overlaid (levels: 2300, 3400, 4400, 5500, and 6600 LAEs per pMpc^2). White circles are all bright submillimeter sources observed in our survey without an observed spectral line. Sources spectroscopically confirmed to be protocluster members are plotted with a white star and have alphabetical labels. Bottom: the CO (3–2 in most cases) transitions of 18 SMGs in the HS 1549 protocluster. The galaxies are organized and labeled in order of ascending redshift, starting with “A.” The continuum levels of all galaxies are scaled to the same height; see Appendix B for the full detailed spectra.

6 under a Cycle 6 program (2019.1.00403.S; PI: S. Kikuta) targeting a $6' \times 4'$ region around the central QSO. Observations were obtained on 2019 November 28 in a 40–2 array configuration with baseline lengths of 15–459 m, giving a naturally weighted synthesized beam size of $1''.6$. There were 40 antennas available, with a total on-source integration time of 10 minutes per pointing. Ceres and J2357–5311 were used as flux and phase calibrators, respectively. The data were reprocessed using CASA and the standard ALMA-supplied

calibration, using natural beam weighting to maximize point-source sensitivity. The average 233 GHz continuum sensitivity in the map is $66 \mu\text{Jy}$.

The frequency setting adopted for these observations covers the redshifted CO(8–7) transition around an observed frequency of 239 GHz. Three of the bright SCUBA-2 sources found within the ALMA mosaic have strong CO(8–7) detections above 7σ . These include the two central sources described by K. M. Lacaille et al. (2019; “K” and “L”) and an

Table 1
Observed Properties of the SMGs Ranked in Order of Ascending Redshift

ID	R.A. (J2000)	Decl. (J2000)	z	S_{450} (mJy)	S_{850} (mJy)	$S_{1.4}$ (mJy)	$S_{3.3}$ (μ Jy)
A	15:53:02.6	19:17:33.0	2.758	...	9.8 ± 0.6	...	60 ± 30
B	15:51:17.8	19:17:58.3	2.822	27.9 ± 4.4	11.0 ± 0.3	1.74 ± 0.04	120 ± 30
C	15:52:41.4	19:15:10.0	2.823	37.5 ± 11.8	8.1 ± 0.4	0.75 ± 0.04	<80
D	15:52:22.6	19:11:19.8	2.829	23.9 ± 10.3	9.6 ± 0.4	1.01 ± 0.04	70 ± 30
E	15:52:03.3	19:12:51.3	2.834	17.9 ± 5.0	8.3 ± 0.3	1.45 ± 0.04	60 ± 30
F	15:53:26.5	19:10:16.8	2.838	...	17.3 ± 0.7	0.92 ± 0.05	...
F*	15:53:26.9	19:10:20.6	2.29 ± 0.05	...
G	15:51:52.4	19:11:03.8	2.847	29.3 ± 3.7	8.8 ± 1.0	3.40 ± 0.07	110 ± 30
H	15:52:53.6	19:13:18.2	2.848	55.0 ± 15.3	12.4 ± 0.4	2.78 ± 0.05	130 ± 30
I	15:52:03.4	19:10:01.3	2.851	24.1 ± 5.6	9.0 ± 0.4	1.99 ± 0.05	<70
J	15:52:12.9	19:11:16.3	2.853	20.7 ± 5.1	8.6 ± 0.3	0.70 ± 0.04	70 ± 30
J*	15:52:12.8	19:11:21.3	1.15 ± 0.04	...
K	15:51:53.2	19:10:59.5	2.854	29.3 ± 3.7	5.6 ± 1.1	1.34 ± 0.07	<70
L	15:51:53.8	19:11:09.7	2.855	16.4 ± 3.8	9.4 ± 1.1	3.37 ± 0.07	160 ± 20
M	15:51:10.1	19:14:00.8	2.865	14.8 ± 5.9	8.0 ± 0.4	1.39 ± 0.05	<100
N	15:53:10.4	19:13:32.4	2.868	...	11.4 ± 0.6	2.26 ± 0.05	50 ± 30
O	15:51:19.9	19:17:31.2	2.872	12.9 ± 4.6	8.0 ± 0.3	2.03 ± 0.05	70 ± 30
P1	15:52:41.8	19:14:26.6	2.891	33.8 ± 11.7	8.2 ± 0.4	1.16 ± 0.05	50 ± 20
P2*	15:52:41.9	19:14:40.2	2.893	0.45 ± 0.05	40 ± 30
Q	15:51:49.5	19:10:41.1	2.923	8.6 ± 3.8	4.9 ± 0.2	0.57 ± 0.09^A	50 ± 30

Note. The R.A. and decl. values are from the 1.4 mm continuum (3 mm and 1.3 mm for “A” and “Q,” respectively), and z is from the CO(3–2) transition. We give the total S_{450} and S_{850} flux densities of each SCUBA-2 source, and we quote all continuum flux densities that are resolved by NOEMA. “A,” “F,” and “N” fall outside the 450 μ m map. When the SCUBA-2 beam is resolved into multiple sources in the 1.4 mm continuum, we denote this by a * (“F,” “J,” and “P2”). The 1.4 mm continuum of “Q” is measured from the ALMA Band-6 map (labeled with ^A). $S_{3.3}$ was not measured for “F,” and 3σ upper limits are quoted for SMGs with a continuum smaller than their sensitivity.

additional source in our bright SMG sample (“Q” in Figure 1). Sources “I” and “E” also happen to fall within the field of view.

3. Analysis

3.1. Measuring Spectral Lines

We ran the Python package `LineSeeker` (J. González-López et al. 2017) on the 3 mm data cubes to find potential spectroscopic lines. This algorithm takes the primary-beam-uncorrected images and convolves them with Gaussian kernels to check for potential lines, with the brightest one corresponding to the redshifted CO(3–2) emission line ($\nu_{\text{rest}} = 345.8$ GHz). We applied a strict signal-to-noise ratio (SNR) selection, where we kept only the candidate spectral lines with SNR higher than the most significant false detection ($\text{SNR}_{\text{negative}} \approx 5$). We then correlated the locations of these potential lines with the corresponding SCUBA-2-identified bright submillimeter source, and all lines outside one SCUBA-2 beam ($r \approx 8''$) were deemed unrelated to the submillimeter source. We also removed all the line-of-sight (LOS) outliers ($\Delta z \geq 0.1$; 10% of the detections), resulting in 17 SMGs spectroscopically identified in CO(3–2). Source “P” has two components, both galaxies lying at a similar redshift. Here, we define multiplicity as resolved high-S/N (>5) sources in the SCUBA-2 beam detected at 1.3/1.4 mm.

We replicated the same methods with the 1.4 mm data, beginning with running `LineSeeker`. The brightest spectral lines observed at this wavelength can be a CO(7–6) line ($\nu_{\text{rest}} = 806.7$ GHz), a CI(2–1) line ($\nu_{\text{rest}} = 809.3$ GHz) or both. The program observed most (16) of the sample SMGs at a higher frequency (excluding “A” and “Q”), introducing an additional SMG “F” to the sample, and bringing the total number of $z \approx 2.85$ SMGs identified up to 18.

We extracted the spectra at the locations of the peak pixels. The NOEMA beam is large with FWHM of $3''.8 \times 2''.7$ at 3 mm and $1''.5 \times 0''.7$ at 1.4 mm, leaving most galaxies unresolved or barely resolved ($\approx 1.5 \times \text{FWHM}$), respectively. Therefore, we quote the higher SNR measurement of peak pixel and aperture photometry. Here, the aperture used is scaled to the FWHM. The observed brightness of each galaxy in the submillimeter is modeled by a combination of its emission from heated dust (modified blackbody radiation) and emission lines from the spectral transitions. Our model for each spectrum is thus

$$\text{Line}(\nu) = B(\nu) + \text{Gauss}_i(\nu, \sigma_{\text{FWHM}}, \mu_i, A_i). \quad (1)$$

Here, $B(\nu)$ is the dust continuum emission (which remains constant for the narrow frequency range of our observation window). We model each emission line with a Gaussian function, where the width of the transition, σ_{FWHM} , is the FWHM of the line, μ_i is the frequency at the peak of the i th line, and A_i is the maximum brightness of the i th line. We introduce a new Gaussian term to the emission function for each transition within the observation window, with one value for the FWHM and redshift across all lines. We have tried modeling each emission line with a double Gaussian model, but we did not find an improvement in the fit. In Table 2, we quote the physical parameters of each galaxy derived from their spectral properties: dynamical mass, M_{dyn} ; cosmological redshift, z ; and gas mass, M_{gas} . The galaxies are organized and labeled in order of increasing redshift in the table. The protocluster field at 850 μ m and the central core (K. M. Lacaille et al. 2019) are shown in Figure 2, with LAE contours (S. Kikuta et al. 2019) overlaid. The bottom of the figure shows the individual spectral lines, in all cases CO(3–2) except for “I”

Table 2

Derived Properties of the SMGs in HS 1549 Ranked in Order of Ascending Redshift

ID	R_{LOS} (pMpc)	SFR ($M_{\odot} \text{ yr}^{-1}$)	M_{gas} ($10^{10} M_{\odot}$)	M_{dyn} ($10^{10} M_{\odot}$)
A	-25.08	1430 ± 80	7.0 ± 1.8	67.0 ± 39.9
B	-7.54	1580 ± 50	7.9 ± 1.7	19.8 ± 7.7
C	-7.27	1170 ± 60	7.0 ± 1.5	25.3 ± 9.3
D	-5.65	1390 ± 60	6.2 ± 1.4	13.6 ± 5.7
E	-4.30	1200 ± 40	10.5 ± 2.3	133.0 ± 50.0
F	-3.22	540 ± 70	7.9 ± 2.0	36.0 ± 9.7
G	-0.80	1270 ± 150	7.8 ± 1.5	27.1 ± 5.3
H	-0.54	1790 ± 60	3.6 ± 1.3	37.4 ± 30.4
I	+0.27	1290 ± 50	3.3 ± 1.0	2.2 ± 0.5
J	+0.80	510 ± 30	3.9 ± 1.2	34.3 ± 21.7
K	+1.07	810 ± 150	2.6 ± 0.7	17.4 ± 8.5
L	+1.34	1360 ± 150	4.1 ± 0.8	6.6 ± 1.8
M	+4.01	1140 ± 50	4.8 ± 1.2	9.2 ± 4.5
N	+4.81	1640 ± 80	6.6 ± 1.6	25.6 ± 12.0
O	+5.87	1140 ± 50	9.0 ± 1.9	48.6 ± 17.9
P1	+10.90	830 ± 40	3.3 ± 0.8	3.2 ± 1.6
P2	+11.43	340 ± 60	6.6 ± 1.5	16.5 ± 7.0
Q	+19.29	690 ± 30	4.3 ± 0.9	3.1 ± 2.0

Note. Here z is measured from spectroscopy, R_{LOS} is the line-of-sight offset (in units of pMpc) from $z = 2.85$, SFR is scaled from the S_{850} flux density from Table 1, M_{gas} is scaled from CO line strength (Table B1), and M_{dyn} is scaled from the CO line width (Table B1).

where we show the higher-SNR CO(8–7) line from ALMA, revealing the shift in velocity across the sample. The redshift distribution is shown in the top-right panel of Figure 3. Individual continuum maps and spectral lines for each SMG are shown in Appendix B.

3.2. Redshift Estimates

Spectroscopy gives precise measurements of the redshift of each galaxy. By knowing which transition we are observing, we can calculate the redshift of photons using

$$z = \frac{\nu_{\text{rest}}}{\nu_{\text{obs}}} - 1. \quad (2)$$

Here, ν_{rest} and ν_{obs} are the rest and observed frequencies of the spectral transition, respectively. We can rule out interloper lines in the SCUBA-2 beam by observing different spectral transitions from the same galaxy. We consider galaxies as protocluster members if we have detected both their CO(3–2) and CO(7–6) or CI(2–1) emission lines, otherwise we require the spectral line to have high SNR > 5.5 (above the LineSeeker significance threshold) for galaxies with only a single line detection (namely the ALMA source “I” with $\text{SNR}_{\text{CO}(8-7)} = 10.2$, and sources “A” with $\text{SNR}_{\text{CO}(3-2)} = 5.5$ and “F” with $\text{SNR}_{\text{CO}(7-6)} = 8.2$). The redshifts of all the galaxies are shown in the fourth column of Table 1. We note that although we select protocluster members from a set of strict criteria (detection of at least one spectral line, $\Delta z < 0.1$, and having a SCUBA-2 counterpart), most of the identified galaxies are far away from the barycenter and the QSO (see Figure 4).

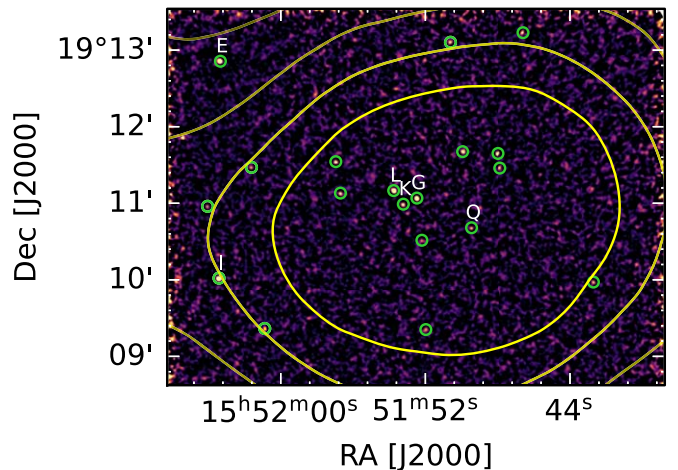


Figure 2. Central region of HS 1549, showing deep ALMA Band-6 (240 GHz) imaging (PI: Kikuta). The same LAE contours (S. Kikuta et al. 2019) are overlaid in yellow on the ALMA image. Galaxy “G,” the QSO, is in this central region. The green circles represent sources found with a 4.5σ detection threshold, and their flux densities are given in Appendix A.

3.3. SMGs in HS 1549

We used NOEMA to search for the $^{12}\text{CO}(3-2)$ transition near the median protocluster redshift of 2.85, revealing 16 $z \approx 2.85$ line emitters at a high SNR (>5) from 15 unresolved SCUBA-2 sources (source P breaks up into two SMGs: “P1” and “P2”). Together with two previously discovered $S_{850} \sim 5$ mJy sources with CO(3–2) redshifts (K. M. Lacaille et al. 2019; S. C. Chapman et al. 2023) this forms a sample of 18 bright SMGs in the HS 1549 protocluster. Follow-up observations with NOEMA identified that 14 of the SMGs also had CO(7–6) or/and CI(2–1) line detection(s). All of the galaxies are individually detected in continuum at $>5\sigma$, either through NOEMA Band-3 maps or the ALMA Band-6 map (also reported as 1.4 mm, with average continuum rms of $66 \mu\text{m}$), with the continuum flux density of SMGs ranging from 0.4 to 2.1 mJy at 1.4 mm (Table 1). Excluding the protocluster SMGs, we find the number counts (not in the HS 1549 structure) are around 30 deg^{-2} , which is comparable to typical number counts of the brightest SCUBA-2 sources in the blank field (A. Weiß et al. 2009; J. E. Geach et al. 2017).

Most of the SCUBA-2 sources outside the core region are resolved as a single bright object with NOEMA, with only three sources breaking into two galaxies of roughly equal flux density, thus representing a low source multiplicity (3/15 or 20%) for such bright SMGs. HyLIRG SMGs in the field are relatively rare, although the density of bright sources varies between different fields. R. Hill et al. (2018) selected bright field SMGs ($S_{850} > 10$ mJy) and found a similar source multiplicity (15%). This is in contrast with the field SMGs from S. M. Stach et al. (2018) and J. M. Simpson et al. (2020), where 30%–53% of bright $850 \mu\text{m}$ sources break up into multiples at similar depths to our data (≈ 1 mJy at $850 \mu\text{m}$). The difference can potentially be explained by the lower sensitivity of the interferometry observations from NOEMA compared to the ALMA observations.

3.4. Gas Mass Estimates

In Table 2, we give the gas mass of each galaxy. The gas mass measures the size of the gas reservoir, which is

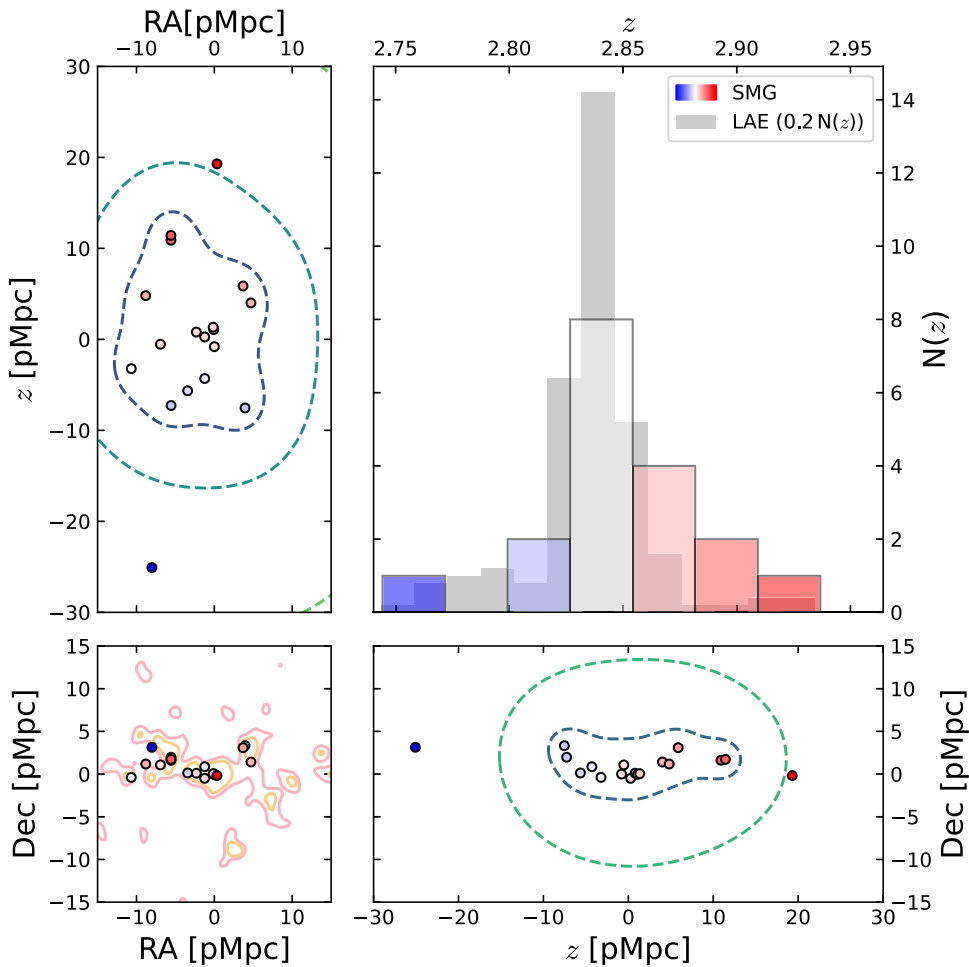


Figure 3. Four different projections of the three-dimensional structure of HS 1549. Bottom left: the on-sky projection of the 18 spectroscopically confirmed SMGs in HS 1549, plotted in R.A. and decl. The contours shown are from the LAE surface density distribution (S. Kikuta et al. 2019; K. M. Lacaille et al. 2019), and we find the SMGs situated in the highest-density regions. Top left: the projection of HS 1549 as seen from the “top” perspective, in R.A. and redshift. The contours are drawn from the distribution of the SMGs, showing the structure’s shape. Bottom right: the projection of HS 1549 as seen from the “side” perspective, in decl. and redshift. The SMGs trace a structure extended along the redshift axis and compressed along the decl. axis. Top right: the one-dimensional histogram of the spectroscopic redshifts. The distribution peaks around $z \approx 2.85$, which we use to define the mean redshift of HS 1549. We compare with the LAE redshift distribution (scaled by a factor of 0.2) and find that SMGs and LAEs peak around the same redshift ($z = 2.852 \pm 0.025$). In all panels, SMGs are color-coded by their redshifts; redder galaxies have higher redshifts.

predominantly H_2 . We apply the relation

$$M_{\text{gas}} = \alpha_{\text{CO}(1-0)} L'_{\text{CO}(1-0)} \quad (3)$$

to scale the line strength, L'_{CO} , to the gas mass. Since we measure the higher J transitions ($J = 3$ and $J = 7$), we first scale the observed line strengths to the ground state, $J = 1$, by applying standard $r_{3,1}$ (0.52 ± 0.09) and $r_{7,1}$ (0.18 ± 0.04) scaling ratios (M. S. Bothwell et al. 2013). We then assume an $\alpha_{\text{CO}(1-0)}$ of $1 M_{\odot} (\text{K km s}^{-1} \text{pc}^2)^{-1}$ to derive the gas mass. It has been shown (N. Sulzenauer et al. 2021) that $r_{i,1}$ depends on the sample of galaxies selected. However, we simply quote the gas mass using the ratios from M. S. Bothwell et al. (2013) for easier comparisons with other protocluster samples. The weighted average of r_{37} ($L'_{\text{CO}(3-2)}/L'_{\text{CO}(7-6)}$) for HS 1549 is 3.06 ± 0.22 , which is comparable to 2.89 ± 0.55 found by M. S. Bothwell et al. (2013).

3.5. Dynamical Mass Estimates

The dynamical mass of a galaxy, M_{dyn} , is the mass calculated by assuming virial equilibrium and measures the mass required

to keep a test particle in a circular orbit with a measured velocity at a given radius. The difficulty of modeling the dynamics of the galaxies requires us to assume some underlying physical distribution of matter in three-dimensional space. We approach quantifying the dynamical mass using the equation (A. Gnerucci et al. 2011)

$$M_{\text{dyn}} \sin^2(i) = f \frac{\sigma_{\text{FWHM}}^2 r}{G}, \quad (4)$$

where i is the inclination angle, f is the correction fraction for a disk galaxy, σ_{FWHM} is the FWHM of the line, r is the galaxy’s half-light radius, and G is the gravitational constant. We assume an average $\langle \sin(i) \rangle = \pi/4$ (D. R. Law et al. 2009, Appendix A) and f of 1.54 (M. S. Bothwell et al. 2013). Typically, r is calculated by fitting a disk profile to the continuum image of the galaxy or fitting a three-dimensional ring profile to the data cube. However, because we lack the spatial resolution required to fully resolve the galaxy, we assume an average r value of 7 kpc (R. J. Ivison et al. 2011). The list of M_{dyn} values can be found in the last column of Table 2, ranging from 10^{10} to $10^{12} M_{\odot}$.

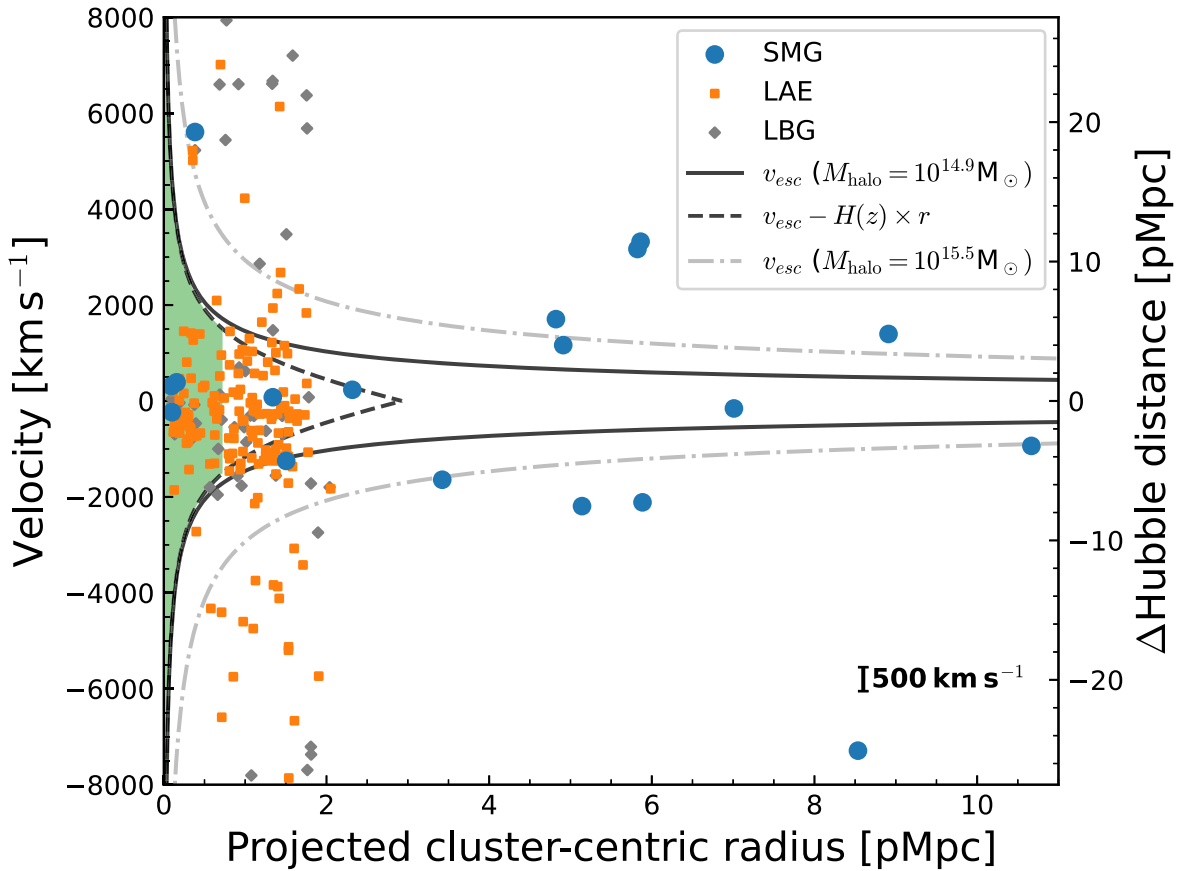


Figure 4. LOS velocity as a function of projected on-sky clustercentric radius. The left axis shows the LOS velocity centered at $z = 2.85$, and the right axis shows the cosmological distance in proper megaparsecs. The blue circles are the spectroscopically confirmed SMG members of the protocluster. The orange squares are LAEs, and the red diamonds are Lyman-break galaxies (C. C. Steidel et al. 2025, in preparation). The solid black curve shows the escape velocity of a dark matter halo of mass equal to $7.4 \times 10^{14} M_{\odot}$ ($v_{200} = 2100 \text{ km s}^{-1}$) and defines a region where objects are likely gravitationally bound to the protocluster. The dashed curve includes the correction from cosmological expansion. The dashed-dotted curve represents the escape velocity of the most massive halos ($3 \times 10^{15} M_{\odot}$ with $v_{200} = 3300 \text{ km s}^{-1}$, e.g., the Phoenix cluster; L. Gao et al. 2012). These curves of escape velocity have been reduced by a factor of $\sqrt{3}$ so that they can be treated as LOS velocities. The green shaded region represents the central area within R_{200} ; the velocities of these galaxies should be dominated by their peculiar motions.

Comparing the dynamical mass to gas mass, we found the median of the ratio is $4.1^{+5.7}_{-3.1}$. We present the median of the ratio, instead of the ratio of each galaxy, because of the large uncertainties from the measurements and the implicit distribution of inclination angles and α_{CO} conversion ratios. This ratio is roughly consistent with the Planck Collaboration et al. (2020) result of there being five times more dark matter in the Universe than baryonic matter. The ratio is close to 5, which also means that the baryonic matter of these galaxies is strongly gas-dominated at $z = 3$ (e.g., T.-M. Wang et al. 2022; A. de Graaff et al. 2024).

3.6. Star Formation Rate Estimates

The far-infrared (FIR) brightness for high-redshift galaxies correlates with the instantaneous SFR because star formation produces dust. Dust naturally absorbs optical starlight and thermally reradiates it at FIR wavelengths. The FIR photons are then redshifted into the millimeter/submillimeter regime. The “total” thermal emission of the dust, known as the total FIR luminosity, or L_{FIR} , is found by fitting FIR photometry to an SED and integrating, conventionally, from 42 to 500 μm . We assume that the SED is well modeled by a modified blackbody. L_{FIR} is then converted to SFR using the functional form (R. C. J. Kennicutt 1998) assuming a Chabrier initial mass

function (G. Chabrier 2003)

$$\text{SFR}[M_{\odot} \text{ yr}^{-1}] = 0.95 \times 10^{-10} L_{\text{FIR}}[L_{\odot}]. \quad (5)$$

Our observations cover four photometry measurements in the FIR to millimeter regime, namely 3.3 mm, 1.4 mm (1.3 mm for ALMA), 850 μm , and 450 μm (we mainly focus on 1.4 mm and 850 μm). The first two measurements trace the Rayleigh–Jeans tail, and at redshifts of around 2.85, the 850 and 450 μm observations begin to trace the peak of the blackbody (more so at 450 μm than at 850 μm). However, the SCUBA-2 map generally has worse effective sensitivity to these galaxies at 450 μm than at 850 μm , with a variable noise across the map due to differing atmospheric transparency through the nights the cluster was observed, resulting in low constraining power of the SED shape from the 450 μm photometry. Our SMGs have an average $S_{850}/S_{1.4} = 5.4 \pm 2.2$, which is expected of a typical SED of SMGs (see A. M. Swinbank et al. 2014).

To more easily compare with other protocluster samples, we scale SFRs from the 850 μm photometry of our HS 1549 SMGs, using a modified blackbody with a dust temperature of 40 K and an emissivity index of 2 (A. M. Swinbank et al. 2014; E. da Cunha et al. 2015) and assuming optically thick dust. In the cases where our NOEMA data resolve the SCUBA-2 source into multiple sources in the 1.4 mm continuum (“F,”

“J,” and “P”), we scale the 850 μm flux densities by their 1.4 mm flux density fractions.

Integrating the modified blackbody function gives the total L_{FIR} , which we convert to SFR (R. C. J. Kennicutt 1998). The uncertainty in our quoted SFR is based purely on the 850 μm photometry, but we note that SFR is also highly dependent on the significant uncertainty in dust temperatures (i.e., a decrease of 5 K reduces the SFR by 50%). However, we adopt the same modified blackbody for all galaxies, limiting the impact of this uncertainty when comparing SFRs to other protoclusters.

4. Results

4.1. Velocity Dispersion of the Protocluster

We calculate LOS velocities relative to the central redshift using

$$v_i = H(z_{\text{cluster}})d_p, \\ d_p = \frac{d_C(z) - d_C(z_{\text{cluster}})}{1 + z_{\text{cluster}}}, \quad (6)$$

where galaxies moving away from us have a positive velocity. Here H is the Hubble parameter, d_p is the proper distance (see Table 2), d_C is the comoving distance, z_{cluster} is the median cluster redshift (2.85), and z is the redshift. However, what we measure (z_{obs}) is the product of the peculiar and cosmological redshifts, $(1 + z_{\text{obs}}) = (1 + z_{\text{pec}})(1 + z_{\text{cosmo}})$. We interpret z_{cosmo} as a measure of distance and z_{pec} as peculiar velocities. In comoving units (cMpc), the cosmological distance is the difference between the SMG and the “center,” defined as the barycenter of the structure. Combining the R.A., decl., and cosmological distance allows us to define a three-dimensional coordinate system.

Within a core region surrounding the QSO (SMGs “G,” “K,” and “L” fall within this region of phase space), the clustercentric redshift of galaxies is likely to be dominated by their peculiar motions, resulting in their LOS clustercentric distances being uncertain. By contrast, at large clustercentric radii, where even a halo with a mass of $\sim 10^{14} M_{\odot}$ has a small escape velocity, z_{cosmo} from the Hubble flow dwarfs the expected $\sim 500 \text{ km s}^{-1}$ peculiar velocities, and their redshifts can be interpreted as distances. The galaxies with the most extreme radii (i.e., “A” and “Q”) may not necessarily be gravitationally bound to the virialized cluster by redshift zero, although they are still affected by the gravitational potential of the growing protocluster.

In Figure 4, we plot the LOS velocities of the SMGs as a function of their clustercentric distances. The radial distance is determined by the straight line between the cluster’s center and each SMG, with the on-sky separation scaled to a length using the angular diameter distance. However, the Hubble flow will not affect some galaxies, i.e., they are already bound to the cluster. We determine the subset of these galaxies using the criterion that they must fall within R_{200} , the radius at which the density of the cluster falls to 200 times the critical density of the Universe at the given redshift. The critical density is given by

$$\rho_{\text{crit}} = \frac{3H^2(z_{\text{cluster}})}{8\pi G}, \\ R_{200} = \left(\frac{3M_{200}}{800\pi\rho_{\text{crit}}} \right)^{1/3}. \quad (7)$$

We assume an upper bound to the mass, $M_{200} = 7.4 \times 10^{14.2} M_{\odot}$, to be the dark matter halo mass of the protocluster (C. C. Steidel et al. 2025, in preparation), defined by an escape velocity profile

that contains 95% of the UV-selected galaxies within a broad $\pm 3000 \text{ km s}^{-1}$ envelope.

The region of the cluster within R_{200} is shaded in light green in Figure 4, with SMGs “G,” “K,” and “L” lying in this region. Assuming the halo mass, M_{200} , we calculate an envelope within which galaxies would be gravitationally bound. We reduce the escape velocity by a factor of $\sqrt{3}$ to be effectively LOS values and then correct for the on-sky Hubble expansion. All the other bright SMGs have observed velocities greater than the escape velocity.

For the central region of the protocluster, there are spectroscopic observations of the LAEs and Lyman-break galaxies (LBGs; C. C. Steidel et al. 2025, in preparation). We also observe substructure across the protocluster (R. F. Trainor & C. C. Steidel 2012) with typical LOS velocities of $250\text{--}300 \text{ km s}^{-1}$ ($\leq 10^{13} M_{\odot}$). We estimate their true velocities by multiplying by $\sqrt{3}$. The LAEs and LBGs are displayed in Figure 4, where most of the population falls within the gravitational envelope of the central dark matter halo. The dashed region removes the cosmic expansion of the Universe from the gravitational envelope.

4.2. 3D Structure of the Protocluster

Figure 3 shows three different 2D projections of the 3D protocluster. For each projection, we collapse the structure along one of the three axes: z , decl., and R.A., forming the on-sky, top, and side perspectives, respectively. The SMGs trace a structure that is compressed along the decl. axis, comparable to the LAEs, and elongated along the redshift axis, assuming redshifts are purely cosmological. We find, somewhat unexpectedly, that the SMGs reside relatively uniformly in projection across the dense LAE region of the protocluster.

The distance measurements become more secure as we move further away from the median redshift, since the expansion of the Universe increasingly dwarfs the peculiar motions of individual galaxies. However, the redshift outliers (“A” and “Q”) could potentially be non-protocluster members, suggesting that there may be less elongation of the structure along the redshift axis than we measure from the full SMG sample. However, the SMGs with the most extreme redshifts (“A” and “Q”) are still likely to be attracted to the protocluster due to the strong gravitational pull of the massive dark matter halo, even if they retain some nonrandom velocity in the cluster by $z = 0$.

To assess the likelihood of SMG membership at the extremes of the redshift distribution, we compare with simulations of overdense structures at a similar redshift (S. I. Muldrew et al. 2015). We compare the fractional number of SMGs in a given 3D radius with the typical size of a protocluster that will ultimately form a cluster at the current epoch. A typical protocluster found in simulations (with descendant $M_{\text{halo}} > 10^{15.2} M_{\odot}$; S. I. Muldrew et al. 2015) has a radius of $(6.8 \pm 1.5) \text{ pMpc}$. We compare this with our protocluster sample and estimate the radius at which we recover 90% of our SMGs under the approximation that the SMGs in our sample have the same stellar mass. This radius is tightly correlated with the radius derived from the dark matter mass. We find that HS 1549 is larger than 99.99% of all protoclusters found in the simulation, and even if we exclude “A” and “Q,” HS 1549 is still larger than 99.78% of all protoclusters. It is unclear what is happening at the locations of these outliers. It could be the case that these SMGs are separating from the protocluster core through the Hubble flow

or that they are situated in a filament of the cosmic web with some streaming velocity that will eventually collapse at a node (i.e., where the protocluster core is located). More likely than not, these sources will not fall into HS 1549's gravitational potential. However, the gravitational effects these galaxies experience from HS 1549 are larger than the average peculiar motion of a galaxy, meaning that they are not typical field galaxies, regardless of their endpoint at $z = 0$ (similar to LBGs with redshifts on the outskirts of the HS 1549 structure). We consider the restricted (and full) sample cases in the following analysis and discussion.

4.3. Shape of the Protocluster

With the SMGs' redshift information providing our third spatial dimension, we attempt to characterize the protocluster's structure to compare with clusters found in simulations. We model the structure by approximating the protocluster as an ellipsoid and constructing its moment-of-inertia tensor. Each element of the tensor is defined by

$$I_{i,j} = \sum_{p=1}^{N_{\text{SMG}}} w_p x_{p,i} x_{p,j}, \quad (8)$$

where $x_{p,i}$ defines the position of galaxy p along the i th axis, and w_p is the weight associated with each galaxy. Intensity (D. Harvey et al. 2021) and mass (M. Velliscig et al. 2015) are common choices for the weight; however, we use a uniform weight for simplicity because our S_{850} measurements are relatively uniform across the field and to account for filamentary structure (C. C. Lovell et al. 2018). Solving the eigenvalue problem of the moment-of-inertia tensor, we can approximate the major, intermediate, and minor axes of an ellipsoid with the square root of the eigenvalues,

$$\begin{aligned} a &= \sqrt{\lambda_1}, \\ b &= \sqrt{\lambda_2}, \\ c &= \sqrt{\lambda_3}, \\ \lambda_1 &\geq \lambda_2 \geq \lambda_3. \end{aligned} \quad (9)$$

The sphericity and triaxiality (M. Velliscig et al. 2015; C. C. Lovell et al. 2018) parameters are defined as

$$\begin{aligned} S &= \frac{c}{a}, \\ T &= \frac{a^2 - b^2}{a^2 - c^2}. \end{aligned} \quad (10)$$

A unitary sphericity, S , is a perfect sphere and the triaxiality, T , would then be undefined. As S approaches zero, the protocluster becomes more disklike. T is a measure of oblateness/prolateness, with a high T representing a more prolate structure.

We quantify the size of the protocluster by interpreting the shape corresponding to the minimal ellipsoid enclosing all the galaxies. Here, we place the ellipsoid's centroid at the mean of the galaxy positions. By measuring the triaxial lengths (4.4, 8.9, and 53.6 pMpc), we can calculate the projected on-sky area (123 pMpc² or 0.15 deg²) and the volume (3600 pMpc³). We can also determine the sphericity derived from this centroid. We find that the shortening of the semiminor axis of the minimum ellipsoid lowers the sphericity down to 0.08, which is

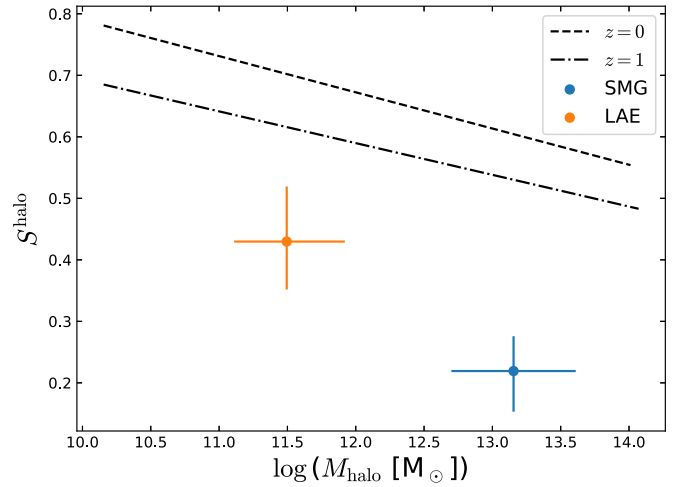


Figure 5. Sphericity of the protocluster compared to subhalo mass. The HS 1549 points are created by solving the moment-of-inertia tensor for the SMGs ($\approx 10^{13.2} M_{\odot}$, in blue) and the LAEs ($\approx 10^{11.5} M_{\odot}$, in orange) with bootstrapped uncertainties. The two dotted black curves are calculated from the inertia tensors in simulated clusters at two different epochs (M. Velliscig et al. 2015); structures at higher redshift are difficult to identify in simulations of restricted sizes. The HS 1549 protocluster is more flattened than typical clusters at lower redshift.

within the uncertainties from the value calculated centered on the QSO (see Figure 5).

In Figure 5, we compare the sphericity of HS 1549 to clusters found in dark matter simulations at different epochs (M. Velliscig et al. 2015). The simulations show a downward trend in sphericity at larger subhalo masses (the halo mass of each galaxy), which we replicate by studying the LAEs, with an average halo mass of $\log(M_{\text{halo}} [M_{\odot}]) = 11.5^{+0.2}_{-0.3}$ (see clustering analysis on LAEs, Y. Herrero Alonso et al. 2023), and the SMGs, with $\log(M_{\text{halo}} [M_{\odot}]) = 13.2 \pm 0.3$ (see clustering analysis on SMGs, S. M. Stach et al. 2021). We do not have spectroscopic data across the entire LAE distribution. Therefore, we calculate the eccentricity (the ratio of the minor to major axis) of the LAEs in the SCUBA-2 map and scale it to the sphericity by calculating the ratio of the eccentricity to sphericity using the SMGs. The uncertainty in sphericity is bootstrapped 10,000 times from the SMGs to account for outliers and propagated to the LAE eccentricity. HS 1549 follows the trend of structures being more disklike at higher redshifts, and the protocluster is flatter than clusters at lower redshift at the same subhalo mass. This suggests a sheetlike collapse of the extended protocluster (C. M. Casey 2016), which is expected early in galaxy cluster formation (see Zeldovich pancakes, Y. B. Zel'dovich 1970), during which matter is streaming in along filaments (J. R. Bond et al. 1996).

5. Discussion

5.1. Radial Profile of SFR in the Protocluster

Given that the SMGs at $z = 2.85$ are found within the region of highest LAE overdensity in the protocluster, understanding how the distributions of SMGs and LAEs compare is of interest. In Figure 6, we show the radial distribution of differential SFR per unit area for the SMGs and the surface density of the LAEs. We derive the surface density of LAEs by taking the counts (S. Kikuta et al. 2019) of the LAEs in each radial bin and dividing by the area of an ellipsoidal shell (with

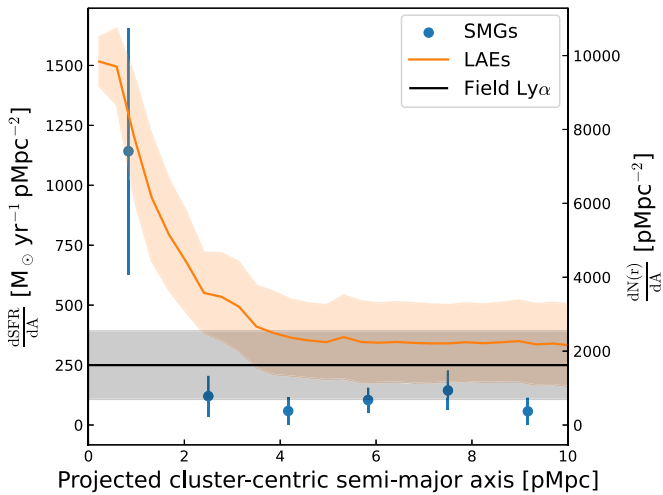


Figure 6. Differential SFR surface density of the protocluster as a function of projected cluster-centric radius. The SMGs are in blue and the LAEs (S. Kikuta et al. 2019) are in orange. The horizontal black region shows the field LAE surface density. The LAEs trace the protocluster with a profile comparable to the SMGs.

eccentricity and position angle derived from solving the moment-of-inertia tensor). The surface density can be scaled to an SFR density using an average SFR for LAEs, $(2.6 \pm 0.8) M_{\odot} \text{ yr}^{-1}$ (Y. Herrero Alonso et al. 2023). We follow a similar procedure for calculating the SFR density of SMGs but truncate the area to overlap with our SCUBA-2 maps. We find that the SMGs trace the LAEs’ profile out to the structure’s edges. The LAE profile also rapidly falls to the average field level of LAEs (≈ 4 pMpc), determined by averaging the LAE density at the edges of the Subaru Hyper Suprime-Cam 1° field.

We then assess the local LAE overdensity around each SMG in HS 1549. The average LAE density in a 1.7 radius around the protocluster SMGs is 4300 pMpc^{-2} (3900 pMpc^{-2} if we exclude the central four SMGs: “G,” “K,” “L,” and “Q”). This corresponds to a 1.6σ (1.5σ) overdensity, which is twice the overdensity found around the non-protocluster SMGs (0.8σ , with a surface density of 3100 pMpc^{-2}). In the case of HS 1549, we usually find SMGs in overdense regions of the $\text{Ly}\alpha$ surface distribution.

5.2. Densities of SMGs and LAEs in the Protocluster

We explore the protocluster environment by comparing the $850 \mu\text{m}$ number counts of the 18 SMGs found in HS 1549 with blank-field counts (J. E. Geach et al. 2017). The galaxies were selected with $\Delta z_{\text{spec}} \leq 0.1$ and the multiplicity corrected by scaling the $850 \mu\text{m}$ flux densities with the 1.4 mm continuum flux densities ($S_{1.4}^{(i)}/\sum S_{1.4}^{(i)}$, extending over an area of 0.15 deg^2).

We find that the SMG number counts ($80 \pm 23.2 \text{ deg}^{-2}$) agree with the blank-field counts ($85.3 \pm 4.6 \text{ deg}^{-2}$) within uncertainties of the counting error. However, in comparison to our limited redshift range ($z = 2.85 \pm 0.1$; 206 cMpc), a blank-field survey in the submillimeter is sensitive to a much wider range of redshifts ($z = 2 \pm 1$; 3100 cMpc) due to the negative- k correction. Assuming the galaxies in the blank field are not clustered and are evenly distributed across the redshift range, we can scale the surface density of the blank field by a factor of 15. The resulting volume density of HS 1549 is a factor of 14.1 ± 4.1 times higher than the field, but with the small survey

($2 \times 10^5 \text{ cMpc}^3$) comes large sample variance, about 25% (S. P. Driver & A. S. G. Robotham 2010). Including the additional source of noise, we find that the volume density of SMGs in HS 1549 is 14.1 ± 5.5 times higher than in the field.

The situation is similar if we consider the surface density of the LAEs in a 1.7 radius around the protocluster SMGs. We find that the LAE surface density is three times higher than the blank sky (1400 ± 600 ; see D. Sobral et al. 2018). This ratio rapidly falls to about 50% higher than the average when we reach the average surface density in HS 1549 (see Figure 6), although this can also be affected by sample variance. The redshift bins for $\text{Ly}\alpha$ surveys are much narrower than for submillimeter surveys, and with both LAE samples having similar selections, we refrain from applying a correction factor when correcting for the volume density.

We can compare the number of SMGs (80 deg^{-2}) to the number of LAEs (2100 deg^{-2}) in HS 1549 and those from the blank sky ($85 \text{ deg}^{-2}/1400 \text{ deg}^{-2}$). We find that the ratios are $(3.8 \pm 2.4) \times 10^{-2}$ for HS 1549 (we only account for the sample variance once, assuming it affects both SMGs and LAEs similarly) and $(6.0 \pm 2.7) \times 10^{-2}$ for the blank field. We can apply the same redshift sensitivity correction ($1/15$) and compare the two ratios to arrive at 9.5 ± 7.4 more SMGs per LAE in HS 1549 than in the field. A higher significance level would be evidence for environmentally driven enhancement of the formation of massive galaxies in protocluster environments. However, the large variance coming from clustering in such a small area, as well as the counting uncertainty in our sample, combined with the uncertain blank-field LAE measurement, limit our ability to measure the ratio at a higher significance level.

We can also consider the difference between the numbers of SMGs in the core of the protocluster ($r_i \leq R_{200}$) and in the outskirts ($r_i > R_{200}$) as a measure of the star-forming environment. In HS 1549, only 3/18 galaxies are situated within the central region, which is in contrast to a recent study from P. Araya-Araya et al. (2024), where simulations showed a more significant number of dust-obscured galaxies in the core region than in the outskirts. If we consider the maximum radius of the protocluster to be around 1.8 pMpc (the radius of a Coma-type protocluster at redshift 3, P. Araya-Araya et al. 2024), we arrive at a similar fraction of 3/5 SMGs in the core of HS 1549. We do not expect the brightest SMGs ($S_{850} > 10 \text{ mJy}$) to be clustered (S. C. Chapman et al. 2015), which is in agreement with our findings. However, these statistics are also plagued by the stochasticity of SMGs (T. B. Miller et al. 2015) and their counting uncertainties. While we observe an overdensity of high-mass galaxies in the overdense protocluster core region, this environment may extend far beyond our current expectations, which the SMGs and LAEs can together trace.

5.3. Protocluster SFR Comparison Sample

To place HS 1549 in context and compare to other systems claimed to be protoclusters, we assemble from the literature various SMG-rich overdensities at $2 < z < 5$. Although a direct comparison of the number counts (number deg^{-2}) of SMG-overdense systems can be performed, it involves making somewhat arbitrary choices of enclosed areas and redshift boundaries.

In Figure 7, we show instead the cumulative $850 \mu\text{m}$ flux density translated to SFR in HS 1549 compared to other

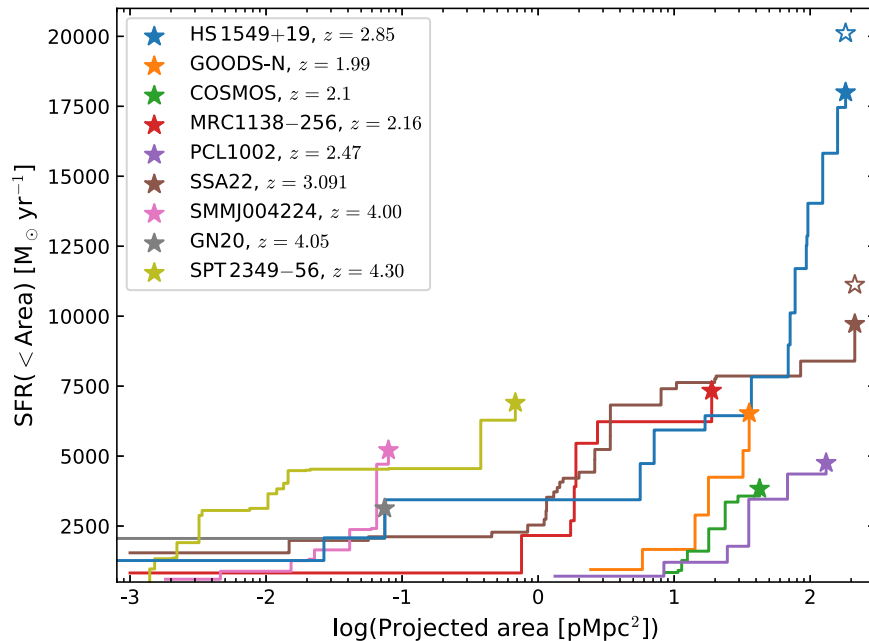


Figure 7. Comparison of $z > 2$ protoclusters: the cumulative SFR from SMGs (selected by SCUBA-2) as a function of the projected on-sky area. For HS 1549, we define the center as the QSO position, with the star representing the total SFR and the hollow star representing the total without the two SMGs with the most discrepant redshifts. Here SFR is scaled from the $850 \mu\text{m}$ flux density of the spectroscopically confirmed SMGs in all the protoclusters shown, assuming $T_{\text{dust}} = 40 \text{ K}$. We show the integrated total SFRs. Protoclusters found in the literature lie in the range $z = 2\text{--}4.3$: GOODS-N (S. C. Chapman et al. 2005; L. L. Cowie et al. 2017); COSMOS (T. Yuan et al. 2014); MRC 1138–256 (the Spiderweb, H. Dannerbauer et al. 2014); PCL 1002 (C. M. Casey et al. 2015); SSA 22 (H. Umehata et al. 2015; S. C. Chapman et al. 2025, in preparation); SMMJ 004224 (Distant Red Core, I. Oteo et al. 2018); GN 20 (E. Daddi et al. 2009; J. A. Hodge et al. 2013; L. L. Cowie et al. 2017); and SPT 2349–56 (T. B. Miller et al. 2018; R. Hill et al. 2020).

published protoclusters found in the literature (S. C. Chapman et al. 2009; E. Daddi et al. 2009; J. A. Hodge et al. 2013; H. Dannerbauer et al. 2014; T. Yuan et al. 2014; C. M. Casey et al. 2015; H. Umehata et al. 2015; T. B. Miller et al. 2018; I. Oteo et al. 2018; R. Hill et al. 2020; for more details, see Appendix C). We assume the same dust temperature of 40 K for all protoclusters. The comparison protocluster data are drawn partially from a recent compilation (see references in C. M. Casey 2016), and partially from primary references. Only galaxies confirmed to be protocluster members via spectroscopic redshifts are considered.

To create the cumulative submillimeter flux distributions for the comparison protoclusters in Figure 7, the center of each protocluster is defined by computing the median R.A. and decl. of all submillimeter sources. We checked that adjusting the centers for the curves randomly by $\sim 1'$ did not change the curves by more than 10%, demonstrating that the curves for the SMG overdensities are fairly insensitive to the adopted center.

Similar to other protoclusters, HS 1549 has an extreme center, but the integrated SFR rises steeply above that of all other high-redshift protoclusters beyond the $2.4\text{--}4.8 \text{ pMpc}$ inner regions, exceeding a total SFR of $1.8 \times 10^4 M_{\odot} \text{ yr}^{-1}$. Furthermore, no other protocluster contains nearly as many bright $S_{850} > 8 \text{ mJy}$ SMGs, and its uniqueness becomes more dramatic if we limit the comparison to only the most luminous SMGs. HS 1549 is also one of the largest protoclusters in the sky. The excess of bright SMGs highlights how hyperluminous infrared galaxies (HyLIRGs) trace the large-scale structure in HS 1549, presumably indicating very rapid galaxy growth.

5.4. Simulations

To understand how rare the observed density of bright SMGs in HS 1549 is, we used the Big MultiDark Planck (BigMDPL)

simulation (F. Prada et al. 2012) at the closest available redshift ($z = 2.89$) to examine the neighboring regions of massive halos. BigMDPL is a dark-matter-only simulation containing 3840^3 N -body particles within a volume 50 cGpc^3 , giving a mass resolution of $3.5 \times 10^{10} M_{\odot}$. This resolution is sufficient to resolve halos of mass $M_{\text{vir}} = 3.5 \times 10^{12} M_{\odot}$ and the volume is large enough that it should provide hundreds of massive group-sized structures at $z \sim 3$.

Based on the estimated central halo mass of HS 1549, $M_{\text{vir,est}} \sim 10^{14} M_{\odot}$, we searched BigMDPL for all halos more massive than $\log(M_{\text{vir,limit}}/M_{\odot}) = 13.8$. We found 435 halos at $z = 2.89$ that satisfy this mass cut. For each massive halo, we searched three separate spherical regions with radii $R = \{20, 30, 40\} \text{ cMpc}$ for neighboring halos. In each spherical region, we ranked all neighboring halos by virial mass and determined the mass of the 10th most massive halo. Ten is chosen as a fiducial baseline, since at least three of the 18 SMGs in HS 1549 lie within the central halo, and at least two of the outlying SMGs likely probe the same halo (e.g., P1/P2 in Table 2). This gives us a minimum mass, $M_{\text{vir,10}}$, above which at least 10 neighbors are equally or more massive.

Figure 8 shows the result of our calculation for $M_{\text{vir,10}}$. We binned the result by the virial mass of the most massive halos in the simulation at $z = 2.89$ and found the median value for each massive halo in the neighborhood, given by R . The shaded regions show the uncertainty for each massive halo. The shading disappears at the high-mass end, where the number of central halos diminishes exponentially until only one halo with greater mass than $10^{14.1} M_{\odot}$ remains.

From clustering analysis of SMGs (S. M. Stach et al. 2021), the typical halo mass of $z = 2\text{--}3$ SMGs is inferred to be $\approx 10^{13} M_{\odot}$. Strictly interpreted, none of the simulated central halos have 10 satellite halos with masses $> 10^{13} M_{\odot}$, even out

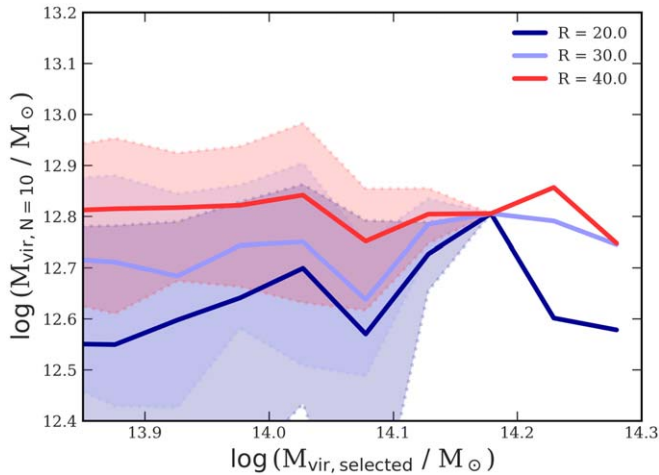


Figure 8. From the BigMDPL simulation (see text), the median mass (vertical axis) of the 10th most massive nearby halo in bins of halo virial mass for all halos above $\log(M_{\text{vir}}/M_{\odot}) = 13.8$ (horizontal axis) at $z = 2.89$. The curves show the mass at which at least 10 halos have equal or greater virial mass within R , for a given selected halo mass $M_{\text{vir,selected}}$. Each colored line shows a different spherical radius in cMpc that was used to find neighboring halos. The shaded regions show a $\pm 1\sigma$ spread around the median for each radius.

to the largest radii considered (40 cMpc). The closest system is a single $10^{14} M_{\odot}$ central halo whose 10th most massive satellite is $9 \times 10^{12} M_{\odot}$. However, any of these simulated central halos do have at least 10 massive satellites within $R < 40$ cMpc, which are massive enough within uncertainties to be viable hosts of SMGs.

For an explicit example, at $R = 20$ cMpc, which would enclose exactly 10 of the HS 1549 SMGs, Figure 8 shows that the most massive central halos in the simulation have a 10th most massive satellite of on average $4 \times 10^{12} M_{\odot}$. Again, while the masses of the satellite halos are, on average, a factor of 2 lower than the mass required to support the SMG halo mass (from field SMG clustering analysis), the masses of satellite halos are not completely out of line with requirements for HS 1549.

The figure demonstrates that very few of the most massive central halos have enough neighboring halos of sufficiently high mass to host the 15 SMGs observed outside the central region of HS 1549. However, the complication in simulating the high density of HyLIRGs in HS 1549 is unlikely the result of the number of available massive halos in simulations, but instead, the star formation prescriptions, feedback recipes, and baryonic physics adopted in simulations.

5.5. HS 1549 in the Context of Cluster Galaxy Evolution

The cores of present-day galaxy clusters contain massive elliptical galaxies with old stellar populations (A. Renzini 2006), and SMGs are believed to be the high-redshift progenitors of these ellipticals (I. Smail et al. 2004; U. Dudzevičiūtė et al. 2020; J. M. Simpson et al. 2020). Therefore, the 18 bright SMGs within a volume of 4400 pMpc^3 are probably set to rapidly become massive elliptical galaxies located within the same structure.

Assuming the individual galaxies' halo masses are characterized by their generally broad central CO(3–2) line widths (Table 2), the implied masses are already comparable to those of cluster ellipticals (with typical masses 10^{10} – $10^{11} M_{\odot}$ by $z \sim 1$; P. Saracco et al. 2014). Thus, a key consequence of our finding is that massive elliptical galaxies can form rapidly at

large clustercentric distances. This conclusion has been found to a lesser extent in other clusters, with fainter SMGs appearing at smaller clustercentric radii near the core (Figure 7). Recent semianalytic models (C. C. Lovell et al. 2018) have indicated that the number of massive galaxies in the wider field correlates strongly with the final descendant cluster mass. In HS 1549, the formation of massive galaxies with high SFRs (up to $1100 M_{\odot} \text{ yr}^{-1}$) over enormous scales (0.24 deg^2) suggests that HS 1549 may be the progenitor of a very massive galaxy cluster.

Theoretical studies have shown that at $z \sim 3$, the progenitors of galaxy clusters should span 5 pMpc ($5000 \text{ kpc} \approx 0.2 \text{ deg} \approx 625''$; Y.-K. Chiang et al. 2014; J. Oñorbe et al. 2014) to 14 pMpc (0.5 deg ; S. I. Muldrew et al. 2015), which is consistent with the observations of LAEs in HS 1549. Observing so many HyLIRGs over these large scales in HS 1549 suggests that it is in an evolutionary phase where cold gas flows (A. Dekel et al. 2009) into the highest-density nodes, replenishing the fuel reservoirs for the many short-lived HyLIRGs being observed simultaneously (C. M. Casey et al. 2015; H. Umehata et al. 2019). For some of the protoclusters from the literature, it is still being determined whether an overdensity of bright SMGs extends over such a large scale. However, evidence generally suggests that it does not exist in most systems (as shown in Figure 7). While the core region of HS 1549 is comparable in its SMG-inferred cumulative SFR to other protoclusters, in the projected region beyond 10 pMpc^2 , the SFR of the HS 1549 protocluster is more than double that of any other known protocluster (and many more times if only HyLIRGs are considered). Probing the HyLIRGs over the wide field in protoclusters provides a unique opportunity to study galaxy cluster formation at a crucial evolutionary epoch and may become a well-calibrated metric of descendant cluster mass.

6. Conclusion

We have mapped the high-density LAE regions of HS 1549 at $850 \mu\text{m}$ with SCUBA-2 (W. S. Holland et al. 2013) to explore how SMGs are distributed throughout the protocluster. We show the SCUBA-2 map covering most of the central Ly α overdensity, including 25 sources detected at $850 \mu\text{m}$ with flux densities brighter than 8 mJy over roughly 0.15 deg^2 of the map, or 167 sources per deg^2 . The surface density in bright SMGs represents about $3\times$ the blank-field SCUBA-2 number counts (J. E. Geach et al. 2017). Previously, the central core of HS 1549 was studied with deep SCUBA-2 maps (K. M. Lacaille et al. 2019), which identified $6\times$ the surface density of bright SMGs compared to blank-field surveys. We performed a blind spectral line survey of all 25 $850 \mu\text{m}$ sources with $S_{850} > 8 \text{ mJy}$ and identified 18 SMGs at the protocluster redshift. Our findings are as follows.

1. The brightest sources have SFRs $> 1000 M_{\odot} \text{ yr}^{-1}$, while the total SFR, including all 18 sources, is $> 2.0 \times 10^4 M_{\odot} \text{ yr}^{-1}$. The SMGs have gas masses (M_{gas}) around $10^{10} M_{\odot}$ individually, with dynamical masses (M_{dyn}) being around $10^{11} M_{\odot}$ (Table 2).
2. Redshift distributions of SMGs allow us to measure the line-of-sight distances and the 3D distribution of bright galaxies. We find an almost uniform distribution of bright SMGs across the HS 1549 protocluster.
3. SMGs trace a highly compressed structure along the decl. axis and a more elongated structure along the R.A. and redshift axes, forming an apparent pancake-like structure.

4. Bright SMGs in HS 1549 and the LAE population (Figure 6) trace a similar surface density profile.
5. Protocluster SMGs are located in more LAE-overdense regions than non-protocluster SMGs ($2\times$ more overdense; see also Y. Tamura et al. 2009).
6. The shape of the protocluster can be characterized by a sphericity of around 0.25. The implied sheetlike collapse of the extended protocluster (C. M. Casey 2016) may be evidence that we are observing the early formation of a galaxy cluster (see Zeldovich pancakes; Y. B. Zel'dovich 1970; A. V. Kravtsov & S. Borgani 2012) and the infalling of matter along filaments (J. R. Bond et al. 1996).
7. The surface density of SMGs in HS 1549 is similar to the blank-field counts (J. E. Geach et al. 2017), but is 14 ± 4 times higher when comparing the volume density. The LAE surface density over the entire protocluster is 50% higher than the average, resulting in a 10 ± 7 times higher SMG to LAE ratio found in HS 1549 compared to the field.
8. The integrated SFR of HS 1549 rises steeply above that of all other high-redshift protoclusters beyond the inner regions, exceeding a total SFR of $2 \times 10^4 M_{\odot} \text{ yr}^{-1}$. Furthermore, no other protocluster contains nearly as many bright $S_{850} > 8 \text{ mJy}$ SMGs, and its uniqueness becomes more dramatic if we limit the comparison to only the most luminous SMGs.
9. We searched the simulations for central halos ($M_{\text{selected}} > 6 \times 10^{13} M_{\odot}$) approaching the inferred mass of HS 1549. For each central halo, we looked at the 10 most massive satellite halos within a volume of 50 cMpc^3 comparable to HS 1549. There is a deficit of halos of the typical clustering mass ($\approx 10^{13} M_{\odot}$) to host the SMGs in HS 1549.
10. HS 1549 is larger than 99.99% of all protoclusters found at $z = 2.85$ when compared to simulated protoclusters (S. I. Muldrew et al. 2015).

The discovery of the 18 bright SMGs across the $\sim 0.15 \text{ deg}^2$ field represents a new opportunity to study and understand galaxy cluster evolution. Individually, the SMGs in HS 1549 can evolve into giant elliptical galaxies, which makes HS 1549 one of the most massive galaxy clusters found to date. The discovery of this system also represents a new opportunity to look for these extended protoclusters, as current studies are focused more on the central region/core of the systems. In the future, more comprehensive multiwavelength surveys will help us better understand the astrophysics of HS 1549.

Acknowledgments

This paper makes use of the following ALMA data: ADS/JAO.ALMA#2019.1.00403.S; PI: S. Kikuta. ALMA is a partnership of ESO (representing its member states), NSF (USA) and NINS (Japan), together with NRC (Canada), MOST and ASIAA (Taiwan), and KASI (Republic of Korea), in cooperation with the Republic of Chile. The Joint ALMA Observatory is operated by ESO, AUI/NRAO and NAOJ. The National Radio Astronomy Observatory and Green Bank Observatory are facilities of the U.S. National Science Foundation operated under cooperative agreement by Associated Universities, Inc. G.W., S.C., and D.S., gratefully acknowledge support for this research from NSERC. Part of the

analysis in this work was made possible by SciNet and the Niagara supercomputing cluster. D.R. is supported by the Simons Foundation. I.R.S. acknowledges support from STFC (ST/X001075/1).

Facilities: JCMT (SCUBA-2), NOEMA (Band 1 and 3), ALMA (Band 6).

Software: `aplpy` (T. Robitaille 2019), `astropy` (Astropy Collaboration et al. 2013, 2018, 2022), `LineSeeker` (J. González-López et al. 2017), `matplotlib` (J. D. Hunter 2007), `numpy` (C. R. Harris et al. 2020), `scipy` (P. Virtanen et al. 2020).

Appendix A ALMA Continuum Sources

We apply a 4.5σ cutoff (corresponding to the S/N of the highest negative peak) to find the continuum-detected sources in the ALMA Band-6 program (PI: Kikuta). We report their 1.4 mm flux densities using aperture photometry. The aperture size and position angle were determined by maximizing the SNR of photometry, and the error for each aperture was sampled from 1000 random realizations of the surface brightness. The results are presented in Table A1.

Table A1
Flux-ranked Table of Sources Identified in the ALMA Band-6 Imaging (PI: Kikuta)

ALMA ID	R.A. (J2000)	Decl. (J2000)	$S_{1.4}$ (mJy)	ID
A1	15:52:03.42	19:10:01.34	3.34 ± 0.07	I
A2	15:52:03.34	19:12:51.30	2.90 ± 0.08	E
A3	15:51:52.47	19:11:04.08	2.72 ± 0.08	G
A4	15:51:53.75	19:11:09.96	2.76 ± 0.08	L
A5	15:51:47.98	19:11:39.07	1.97 ± 0.08	...
A6	15:51:49.94	19:11:40.48	1.37 ± 0.08	...
A7	15:51:53.22	19:10:59.32	1.28 ± 0.09	K
A8	15:51:56.96	19:11:32.63	1.26 ± 0.09	...
A9	15:52:00.89	19:09:21.87	0.90 ± 0.07	...
A10	15:51:46.60	19:13:13.71	1.13 ± 0.09	...
A11	15:51:56.70	19:11:07.99	1.17 ± 0.10	...
A12	15:51:49.45	19:10:40.84	0.83 ± 0.07	Q
A13	15:51:50.61	19:13:06.16	0.85 ± 0.09	...
A14	15:51:42.71	19:09:58.26	0.78 ± 0.08	...
A15	15:51:47.88	19:11:27.59	0.88 ± 0.09	...
A16	15:52:01.62	19:11:28.14	0.73 ± 0.07	...
A17	15:52:04.05	19:10:57.62	0.70 ± 0.08	...
A18	15:51:52.19	19:10:31.04	0.63 ± 0.08	...
A19	15:51:51.97	19:09:21.04	0.91 ± 0.10	...

Note. We present the S/N-maximized aperture photometry at 1.4 mm. In the rightmost column, we have indicated the galaxy's ID described in the main body of this paper ("I," "E," "G," "L," "K" and "Q").

Appendix B Spectral Lines of Each SMG

In Table B1 and Figure B1 we show the spectral lines of all the SMGs (CO(3–2), CO(7–6)/[CI]2–1) and their corresponding continuum maps. Spectra are extracted at the peak pixel in the continuum map. For clarity, we have removed the continuum emission from the spectral lines in the figures.

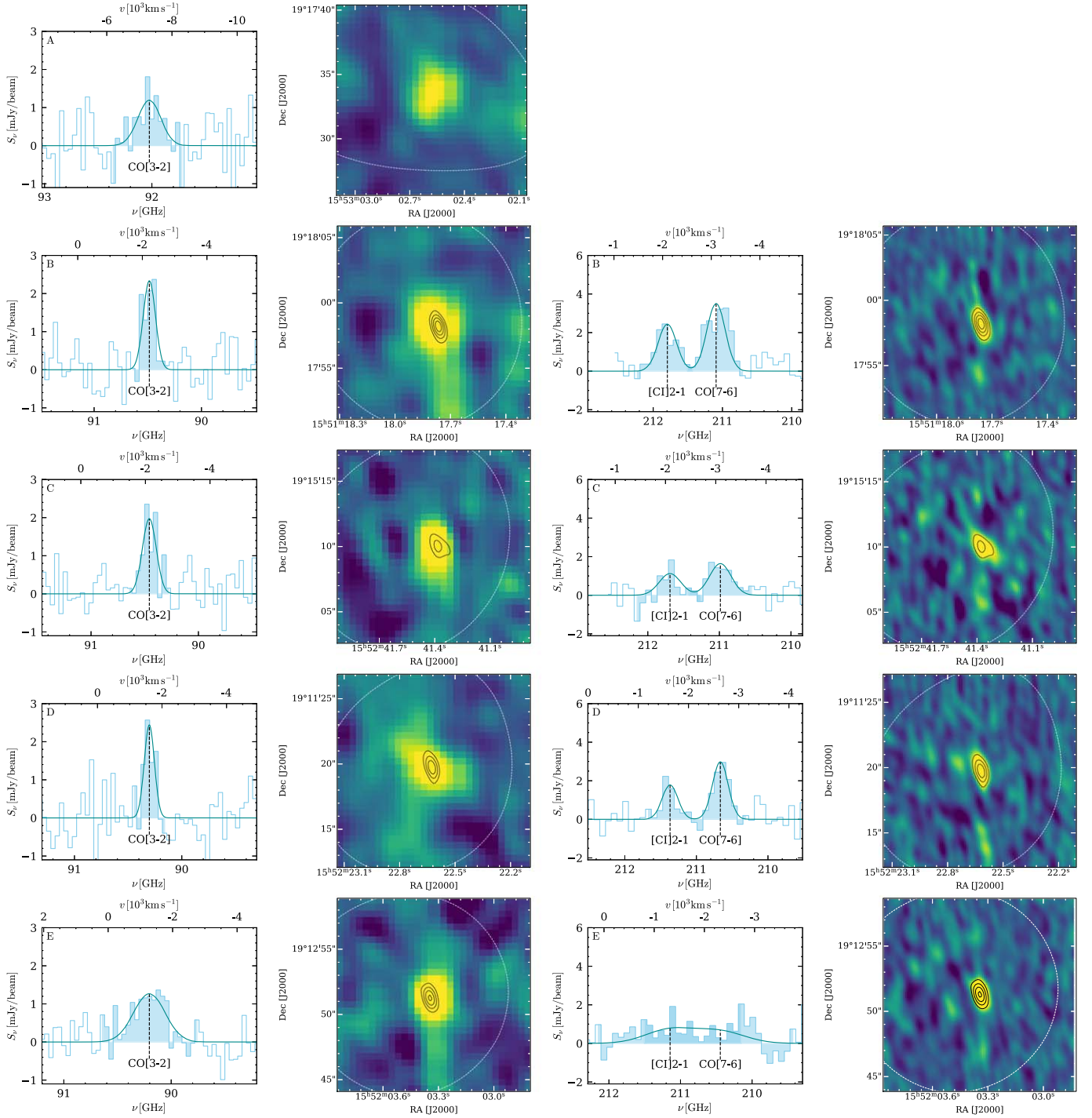


Figure B1. First and second columns: CO(3–2) spectra and channel maps. The 850 μm SCUBA-2 emission is shown by white contours (70% of the peak flux of each source). Identifications within the SCUBA-2 beam are shown with NOEMA 1.4 mm continuum contours in blue (“A” and “Q” were not observed at 1.4 mm). Spectra are extracted at the peak pixel of the channel map constructed from the identified CO(3–2) line. The spectral resolution is 60 km s^{-1} . Gaussian fits to the line profiles are overlaid. Third and fourth columns: CO(7–6)/[CI](2–1) spectra and continuum maps of the subsample followed up with NOEMA at 1.4 mm with spectra extracted at the peak pixel of the 1.4 mm continuum. The 850 μm SCUBA-2 emission is shown by white contours (70% of the peak flux of each source). We show the contours of the 1.4 mm map (4σ , 7σ , 10σ , and 13σ). The spectral resolution is 60 km s^{-1} . Double Gaussian fits to each set of line profiles are overlaid.

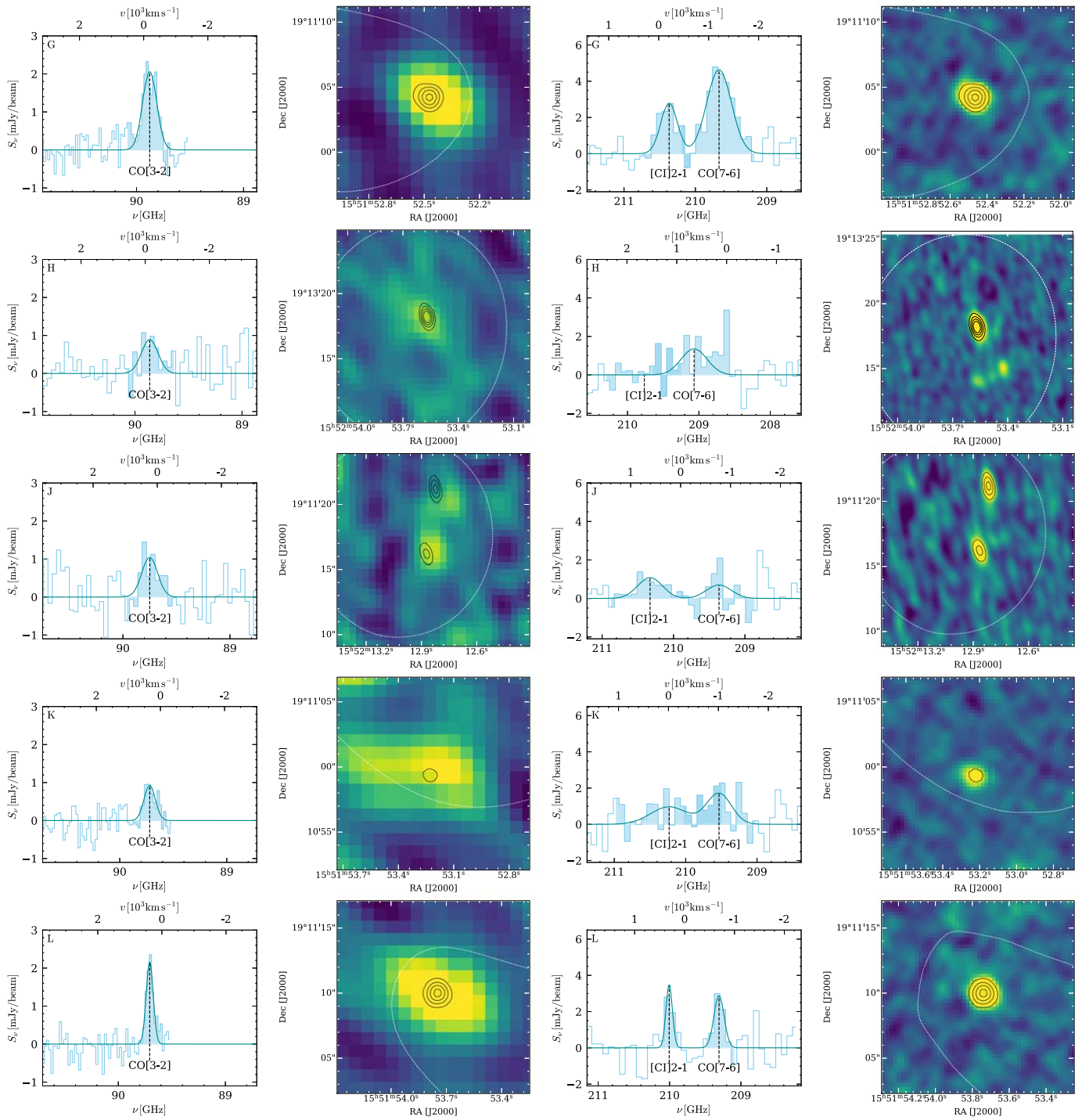


Figure B1. (Continued.)

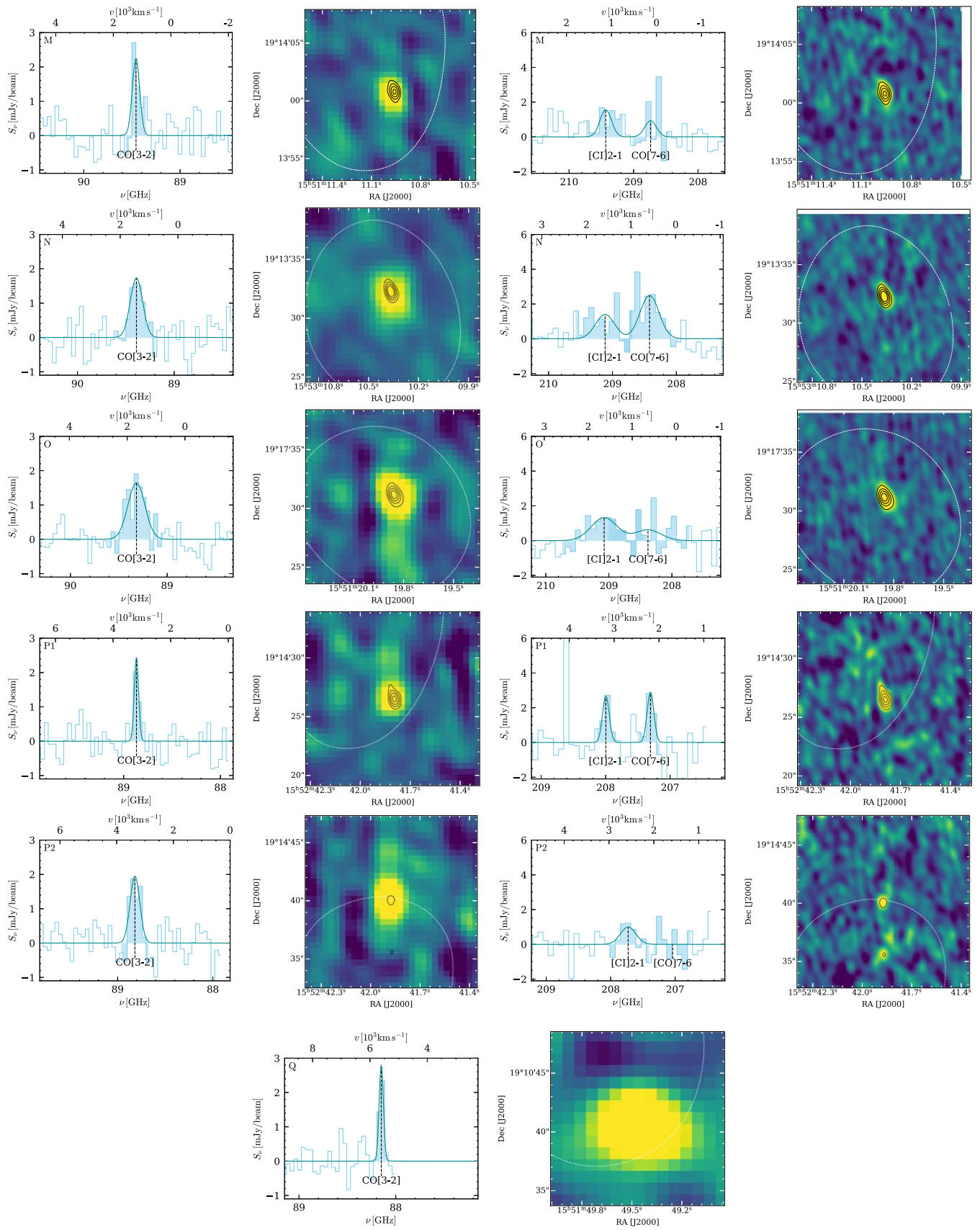


Figure B1. (Continued.)

Table B1

Observed Line Properties of the SMGs Ranked in Order of Ascending Redshift

ID	Line	FWHM (km s ⁻¹)	L_ν (Jy km s ⁻¹)	L' (10 ¹⁰ K km s ⁻¹ pc ²)
A	CO(3–2)	820 ± 240	0.90 ± 0.18	3.62 ± 0.73
B	CO(3–2)	440 ± 90	0.98 ± 0.13	4.08 ± 0.55
	CO(7–6)	...	1.68 ± 0.12	1.28 ± 0.09
	CI(2–1)	...	1.09 ± 0.12	0.83 ± 0.09
C	CO(3–2)	500 ± 90	0.88 ± 0.11	3.65 ± 0.48
	CO(7–6)	...	0.83 ± 0.12	0.63 ± 0.09
	CI(2–1)	...	0.59 ± 0.12	0.45 ± 0.09
D	CO(3–2)	370 ± 80	0.77 ± 0.12	3.20 ± 0.50
	CO(7–6)	...	0.97 ± 0.10	0.75 ± 0.08
	CI(2–1)	...	0.62 ± 0.10	0.47 ± 0.08
E	CO(3–2)	1150 ± 220	1.31 ± 0.17	5.48 ± 0.71
	CO(7–6)	...	0.87 ± 0.18	0.67 ± 0.14
	CI(2–1)	...	0.88 ± 0.18	0.67 ± 0.14
F	CO(7–6)	600 ± 80	1.83 ± 0.22	1.42 ± 0.17
G	CO(3–2)	520 ± 50	0.97 ± 0.07	4.08 ± 0.29
	CO(7–6)	...	2.30 ± 0.30	1.78 ± 0.23
	CI(2–1)	...	1.03 ± 0.27	0.79 ± 0.21
H	CO(3–2)	610 ± 250	0.44 ± 0.14	1.87 ± 0.59
	CO(7–6)	...	0.28 ± 0.16	0.22 ± 0.13
I	CO(8–7)	150 ± 20	1.01 ± 0.08	0.6 ± 0.05
J	CO(3–2)	580 ± 190	0.48 ± 0.12	2.03 ± 0.50
	CI(2–1)	...	0.45 ± 0.13	0.34 ± 0.10
K	CO(3–2)	420 ± 100	0.32 ± 0.06	1.34 ± 0.27
	CO(7–6)	...	0.73 ± 0.24	0.57 ± 0.19
L	CO(3–2)	260 ± 40	0.51 ± 0.05	2.16 ± 0.23
	CO(7–6)	...	0.62 ± 0.15	0.48 ± 0.12
	CI(2–1)	...	0.53 ± 0.13	0.41 ± 0.10
M	CO(3–2)	300 ± 70	0.59 ± 0.10	2.50 ± 0.42
	CI(2–1)	...	0.56 ± 0.12	0.43 ± 0.10
N	CO(3–2)	500 ± 120	0.80 ± 0.14	3.42 ± 0.59
	CO(7–6)	...	1.23 ± 0.45	0.97 ± 0.35
	CI(2–1)	...	0.88 ± 0.15	0.69 ± 0.12
O	CO(3–2)	700 ± 130	1.09 ± 0.14	4.68 ± 0.59
	CI(2–1)	...	0.85 ± 0.19	0.66 ± 0.15
P1	CO(3–2)	180 ± 50	0.40 ± 0.07	1.73 ± 0.30
	CO(7–6)	...	0.65 ± 0.11	0.52 ± 0.09
	CI(2–1)	...	0.35 ± 0.10	0.28 ± 0.08
P2	CO(3–2)	410 ± 90	0.80 ± 0.11	3.45 ± 0.48
	CI(2–1)	...	0.32 ± 0.15	0.26 ± 0.12
Q	CO(3–2)	180 ± 60	0.50 ± 0.06	2.21 ± 0.28

Appendix C**Details of Protocluster Comparison Sample**

The GOODS-N overdensity at $z = 1.99$ (S. C. Chapman et al. 2009) spans a roughly $10' \times 10'$ field in the Hubble Deep Field North, containing six SMGs within $\Delta z = 0.008$. The probability of finding this overdensity from fluctuations in the field distribution is $< 0.01\%$. Interestingly, only a modest overdensity of LBGs is found in this GOODS-N structure.

The COSMOS $z = 2.5$ SMG overdensity (C. M. Casey et al. 2015; PCL 1002) is similar to the GOODS-N structure in terms of the numbers and luminosities of the component SMGs, the angular size of the system, and the modest overdensity of LBGs associated with it.

The MRC 1138 $z = 2.16$ structure was originally discovered as an overdensity of Ly α and H α emitters surrounding a radio-loud active galactic nucleus (AGN) (known as the “Spiderweb Galaxy”) that resides in a large Ly α halo (J. D. Kurk et al. 2000). Follow-up observations (E. Kuiper et al. 2011; H. Dannerbauer et al. 2014; S. Jin et al. 2021) revealed the presence of five SMGs, an additional AGN, and 46 CO line emitters.

The SSA 22 protocluster was one of the first protoclusters discovered by observing an overdensity of LBGs (C. C. Steidel et al. 2000). It is an extended structure (although less extreme than HS 1549) at $z = 3.09$, with LAEs spanning over 50 cMpc (T. Hayashino et al. 2004). Submillimeter observations of the field have revealed a population of many faint SMGs, five of which have $S_{850} > 8$ mJy (S. C. Chapman et al. 2001, 2005, 2023; J. E. Geach et al. 2005, 2017; Y. Tamura et al. 2009; H. Umehata et al. 2015), one of which is a likely outlier comparable to “A” and “Q” in HS 1549.

The COSMOS $z = 2.1$ protocluster (C.-L. Hung et al. 2016) lacks sufficiently deep 850 μm data to characterize the Herschel–SPIRE sources identified in the structure. We estimate 850 μm flux densities by taking their published L_{IR} values (integrated over 3–1100 μm) and using the SED of Arp 220 to establish the scaling relation that $L_{\text{IR}} = 2 \times 10^{12} L_{\odot}$ corresponds to $S_{850} = 1$ mJy at $z = 2.1$.

While more distant than the protoclusters above, and likely having different characteristics, there have also been detections of SMG overdensities at $z > 4$. GN 20 in the GOODS-N field shows signs of a protocluster at $z = 4.05$. It was discovered through the serendipitous detection of CO(4–3) from two SMGs (E. Daddi et al. 2009), with two further SMGs detected subsequently (E. Daddi et al. 2009). An excess of B -band dropouts is also observed in this structure, with several spectroscopically confirmed sources lying at $z \approx 4.05$.

The most luminous example at $z > 4$ is SPT 2349–56 (T. B. Miller et al. 2018), which is characterized by an extremely bright double-lobed LABOCA 870 μm source, resolved by ALMA into 25 SMGs (R. Hill et al. 2020). To this day, no satellite SMGs with bound escape velocities have been found beyond this hyperluminous core region.

Another example is SMMJ 004224, found from a Herschel–SPIRE survey (I. Oteo et al. 2018); it is comparable to SPT 2349–56 but is less concentrated and has a lower total SFR. While an apparent surface overdensity of 870 μm sources was found in the field surrounding SMMJ 004224, most sources lie in the foreground and are not at the protocluster redshift (R. J. Ivison et al. 2020).

ORCID iDs

George C.P. Wang  <https://orcid.org/0009-0003-4626-9777>
 Scott C. Chapman  <https://orcid.org/0000-0002-8487-3153>
 Nikolaus Sulzenauer  <https://orcid.org/0000-0002-3187-1648>
 Frank Bertoldi  <https://orcid.org/0000-0002-1707-1775>
 Christopher C. Hayward  <https://orcid.org/0000-0003-4073-3236>
 Ryley Hill  <https://orcid.org/0009-0008-8718-0644>
 Satoshi Kikuta  <https://orcid.org/0000-0003-3214-9128>
 Yuichi Matsuda  <https://orcid.org/0000-0003-1747-2891>
 Douglas Rennehan  <https://orcid.org/0000-0002-1619-8555>
 Douglas Scott  <https://orcid.org/0000-0002-6878-9840>
 Ian Smail  <https://orcid.org/0000-0003-3037-257X>
 Charles C. Steidel  <https://orcid.org/0000-0002-4834-7260>

References

- Araya-Araya, P., Cochrane, R. K., Hayward, C. C., et al. 2024, *ApJ*, 977, 204
 Astropy Collaboration, Price-Whelan, A. M., Lim, P. L., et al. 2022, *ApJ*, 935, 167
 Astropy Collaboration, Price-Whelan, A. M., Sipőcz, B. M., et al. 2018, *AJ*, 156, 123
 Astropy Collaboration, Robitaille, T. P., Tollerud, E. J., et al. 2013, *A&A*, 558, A33
 Bond, J. R., Kofman, L., & Pogosyan, D. 1996, *Natur*, 380, 603
 Bothwell, M. S., Smail, I., Chapman, S. C., et al. 2013, *MNRAS*, 429, 3047
 Casey, C. M. 2016, *ApJ*, 824, 36
 Casey, C. M., Cooray, A., Capak, P., et al. 2015, *ApJL*, 808, L33
 Chabrier, G. 2003, *PASP*, 115, 763
 Chapin, E. L., Berry, D. S., Gibb, A. G., et al. 2013, *MNRAS*, 430, 2545
 Chapman, S. C., Bertoldi, F., Smail, I., et al. 2015, *MNRAS*, 453, 951
 Chapman, S. C., Blain, A., Ibata, R., et al. 2009, *ApJ*, 691, 560
 Chapman, S. C., Blain, A. W., Smail, I., & Ivison, R. J. 2005, *ApJ*, 622, 772
 Chapman, S. C., Lewis, G. F., Scott, D., et al. 2001, *ApJL*, 548, L17
 Chapman, S. C., Wang, G., & Steidel, C. C. 2023, *ApJL*, 548, L17
 Chiang, Y.-K., Overzier, R., & Gebhardt, K. 2014, *ApJL*, 782, L3
 Cooke, E. A., Smail, I., Stach, S. M., et al. 2019, *MNRAS*, 486, 3047
 Cowie, L. L., Barger, A. J., Hsu, L. Y., et al. 2017, *ApJ*, 837, 139
 da Cunha, E., Walter, F., Smail, I. R., et al. 2015, *ApJ*, 806, 110
 Daddi, E., Dannerbauer, H., Stern, D., et al. 2009, *ApJ*, 694, 1517
 Dannerbauer, H., Kurk, J. D., De Breuck, C., et al. 2014, *A&A*, 570, A55
 de Graaff, A., Rix, H.-W., Carniani, S., et al. 2024, *A&A*, 684, A87
 Dekel, A., Birnboim, Y., Engel, G., et al. 2009, *Natur*, 457, 451
 Driver, S. P., & Robotham, A. S. G. 2010, *MNRAS*, 407, 2131
 Duzdevičiūtė, U., Smail, I., Swinbank, A. M., et al. 2020, *MNRAS*, 494, 3828
 Elbaz, D., Daddi, E., Le Borgne, D., et al. 2007, *A&A*, 468, 33
 Elbaz, D., Dickinson, M., Hwang, H. S., et al. 2011, *A&A*, 533, A119
 Gao, L., Navarro, J. F., Frenk, C. S., et al. 2012, *MNRAS*, 425, 2169
 Geach, J. E., Dunlop, J. S., Halpern, M., et al. 2017, *MNRAS*, 465, 1789
 Geach, J. E., Matsuda, Y., Smail, I., et al. 2005, *MNRAS*, 363, 1398
 Gnerucci, A., Marconi, A., Cresci, G., et al. 2011, *A&A*, 533, A124
 González-López, J., Bauer, F. E., Aravena, M., et al. 2017, *A&A*, 608, A138
 Greve, T. R., Vieira, J. D., Weiß, A., et al. 2012, *ApJ*, 756, 101
 Harris, C. R., Millman, K. J., van der Walt, S. J., et al. 2020, *Natur*, 585, 357
 Harvey, D., Robertson, A., Tam, S.-I., et al. 2021, *MNRAS*, 500, 2627
 Hayashino, T., Matsuda, Y., Tamura, H., et al. 2004, *AJ*, 128, 2073
 Herrero Alonso, Y., Miyaji, T., Wisotzki, L., et al. 2023, *A&A*, 671, A5
 Hill, R., Chapman, S., Scott, D., et al. 2020, *MNRAS*, 495, 3124
 Hill, R., Chapman, S. C., Scott, D., et al. 2018, *MNRAS*, 477, 2042
 Hodge, J. A., Carilli, C. L., Walter, F., Daddi, E., & Riechers, D. 2013, *ApJ*, 776, 22
 Högbom, J. A. 1974, *A&AS*, 15, 417
 Holland, W. S., Bintley, D., Chapin, E. L., et al. 2013, *MNRAS*, 430, 2513
 Hung, C.-L., Casey, C. M., Chiang, Y.-K., et al. 2016, *ApJ*, 826, 130
 Hunter, J. D. 2007, *CSE*, 9, 90
 Ivison, R. J., Biggs, A. D., Bremer, M., Arumugam, V., & Dunne, L. 2020, *MNRAS*, 496, 4358
 Ivison, R. J., Papadopoulos, P. P., Smail, I., et al. 2011, *MNRAS*, 412, 1913
 Jenness, T., Berry, D. S., Cavanagh, B., et al. 2009, in ASP Conf. Ser. 411, *Astronomical Data Analysis Software and Systems XVIII*, ed. D. A. Bohlender, D. Durand, & P. Dowler (San Francisco, CA: ASP), 418
 Jin, S., Dannerbauer, H., Emonts, B., et al. 2021, *A&A*, 652, A11
 Kennicutt, R. C. J. 1998, *ARA&A*, 36, 189
 Kikuta, S., Matsuda, Y., Cen, R., et al. 2019, *PASJ*, 71, L2
 Kravtsov, A. V., & Borgani, S. 2012, *ARA&A*, 50, 353
 Kuiper, E., Hatch, N. A., Miley, G. K., et al. 2011, *MNRAS*, 415, 2245
 Kurk, J. D., Röttgering, H. J. A., Pentericci, L., et al. 2000, *A&A*, 358, L1
 Lacaille, K. M., Chapman, S. C., Smail, I., et al. 2019, *MNRAS*, 488, 1790
 Law, D. R., Steidel, C. C., Erb, D. K., et al. 2009, *ApJ*, 697, 2057
 Lovell, C. C., Thomas, P. A., & Wilkins, S. M. 2018, *MNRAS*, 474, 4612
 Mantz, A. B., Abdulla, Z., Allen, S. W., et al. 2018, *A&A*, 620, A2
 Miller, T. B., Chapman, S. C., Aravena, M., et al. 2018, *Natur*, 556, 469
 Miller, T. B., Hayward, C. C., Chapman, S. C., & Behroozi, P. S. 2015, *MNRAS*, 452, 878
 Mostardi, R. E., Shapley, A. E., Nestor, D. B., et al. 2013, *ApJ*, 779, 65
 Muldrew, S. I., Hatch, N. A., & Cooke, E. A. 2015, *MNRAS*, 452, 2528
 Oñorbe, J., Garrison-Kimmel, S., Maller, A. H., et al. 2014, *MNRAS*, 437, 1894
 Oteo, I., Ivison, R. J., Dunne, L., et al. 2018, *ApJ*, 856, 72
 Planck Collaboration, Aghanim, N., Akrami, Y., et al. 2020, *A&A*, 641, A6
 Prada, F., Klypin, A. A., Cuesta, A. J., Betancort-Rijo, J. E., & Primack, J. 2012, *MNRAS*, 423, 3018
 Renzini, A. 2006, *ARA&A*, 44, 141
 Robitaille, T. 2019, APLpy v2.0: The Astronomical Plotting Library in Python, Zenodo, doi:10.5281/zenodo.2567476
 Rudie, G. C., Steidel, C. C., Trainor, R. F., et al. 2012, *ApJ*, 750, 67
 Saracco, P., Casati, A., Gargiulo, A., et al. 2014, *A&A*, 567, A94
 Simpson, J. M., Smail, I., Duzdevičiūtė, U., et al. 2020, *MNRAS*, 495, 3409
 Smail, I. 2024, *MNRAS*, 529, 2290
 Smail, I., Chapman, S. C., Blain, A. W., & Ivison, R. J. 2004, *ApJ*, 616, 71
 Sobral, D., Santos, S., Matthee, J., et al. 2018, *MNRAS*, 476, 4725
 Stach, S. M., Smail, I., Amvrosiadis, A., et al. 2021, *MNRAS*, 504, 172
 Stach, S. M., Smail, I., Swinbank, A. M., et al. 2018, *ApJ*, 860, 161
 Stanford, S. A., Brodwin, M., Gonzalez, A. H., et al. 2012, *ApJ*, 753, 164
 Steidel, C. C., Adelberger, K. L., Shapley, A. E., et al. 2000, *ApJ*, 532, 170
 Steidel, C. C., Bogosavljević, M., Shapley, A. E., et al. 2011, *ApJ*, 736, 160
 Sulzenauer, N., Dannerbauer, H., Díaz-Sánchez, A., et al. 2021, *ApJL*, 923, L27
 Swinbank, A. M., Simpson, J. M., Smail, I., et al. 2014, *MNRAS*, 438, 1267
 Tamura, Y., Kohno, K., Nakanishi, K., et al. 2009, *Natur*, 459, 61
 Trainor, R. F., & Steidel, C. C. 2012, *ApJ*, 752, 39
 Tran, K.-V. H., Moustakas, J., Gonzalez, A. H., et al. 2008, *ApJL*, 683, L17
 Umehata, H., Fumagalli, M., Smail, I., et al. 2019, *Sci*, 366, 97
 Umehata, H., Tamura, Y., Kohno, K., et al. 2015, *ApJL*, 815, L8
 Velliscig, M., Cacciato, M., Schaye, J., et al. 2015, *MNRAS*, 453, 721
 Virtanen, P., Gommers, R., Oliphant, T. E., et al. 2020, *NatMe*, 17, 261
 Wang, T., Elbaz, D., Daddi, E., et al. 2016, *ApJ*, 828, 56
 Wang, T.-M., Magnelli, B., Schinnerer, E., et al. 2022, *A&A*, 660, A142
 Weiß, A., Kovács, A., Coppin, K., et al. 2009, *ApJ*, 707, 1201
 Yuan, T., Nanayakkara, T., Kacprzak, G. G., et al. 2014, *ApJL*, 795, L20
 Zel'dovich, Y. B. 1970, *A&A*, 5, 84